Abstract

Title of Dissertation:	Signal Corrections and Calibrations of the LUX Dark Matter Detector
	Richard Knoche, Doctor of Philosophy, 2016
Dissertation directed by:	Professor Carter Hall,Department of Physics
	Department of Physics

Abstract Blah

Signal Corrections and Calibrations of the LUX Dark Matter Detector

by

Richard Knoche

Dissertation submitted to the Faculty of the Graduate School of the University of Maryland, College Park in partial fulllment of the requirements for the degree of Doctor of Philosophy

2016

Advisory Committee:

Professor Carter Hall, Chair/Adviser

Professor Person One

Professor Person Two

Professor Person Three

Professor Person Four

Acknowledgments

Acknowledgments Blah

Contents

List of Tables

List of Figures

1 Introduction to Dark Matter

In recent decades it has been discovered that the luminous matter which scientists have studied for centuries is only a small fraction of the total composition of the universe. There is strong evidence for dark baryonic matter (a few percent), non-baryonic hot dark matter ($\sim$0.1%-1.5%), non baryonic cold dark matter ($\sim$27%), and dark energy ($\sim$68%) components to the universe, where the percentages are as a fraction of their total contribution to the universe's composition [23]. While we know a large amount about the "normal" matter which contributes $\lesssim 5\%$ of the universe's total composition, we know very little about these larger components. In particular, while we understand certain characteristics of the cold dark matter component, there is no consensus on its composition. Before examining the experiments which seek to answer this question, we will first discuss what is currently known about nonbaryonic dark matter.

1.1 Evidence for Dark Matter

1.1.1 Mass Measurements from Galactic Rotation Curves

In the early 1930's Fritz Zwicky was the first to use the Virial theorem to determine the total mass of the Coma cluster of galaxies. In his examination, Zwicky found that the velocities at large radii were too high to be consistent with the Newtonian prediction arising from the visible matter alone [59]. This discrepancy was reinforced in the 1970's, when further data on the rotational velocity of spiral galaxies began to be collected. Instead of the rotational velocity falling off as $\propto 1/\sqrt{r}$ beyond the radius of visible matter as one would expect, the rotational velocity rises for small radii, then asymptotes to a constant $v \simeq 100 - 300$ km/s for large radii in most galaxies [43, 26, 17]. The most widely accepted explanation of this phenomenon is that the disk galaxies are immersed in a dark matter (DM) halo such that $M(r)/r$, where $M(r)$ is the total mass within a radius r, remains constant at large radii. Such a halo could form from an isotropic sphere of an ideal gas at a uniform temperature.

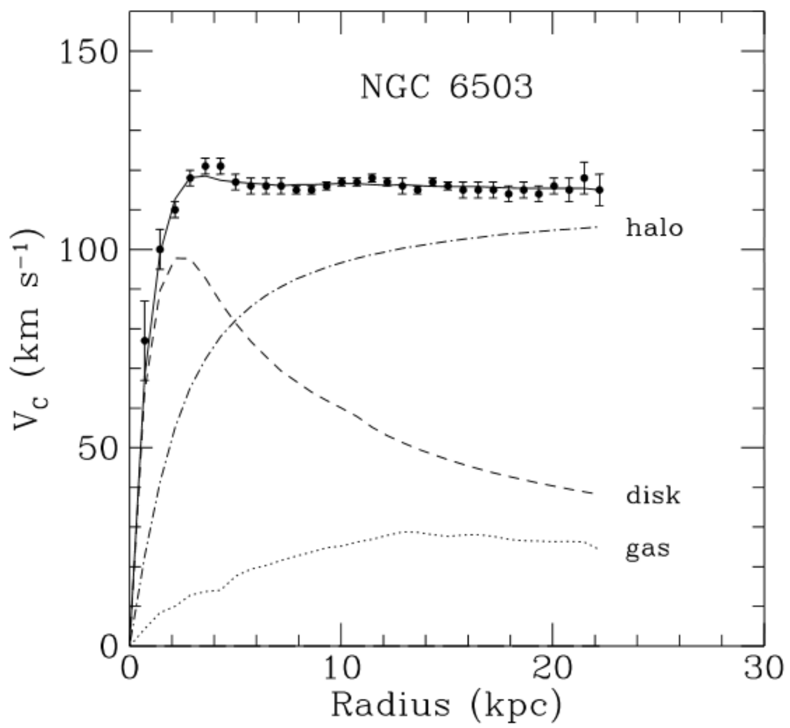

Figure 1: Rotation curve of galaxy NGC 6503. The dotted line indicates the contribution of baryonic gas, the dashed line indicates the contribution of visible matter in the disk, and the dash-dotted line indicates the contribution of dark matter. In the absence of dark matter the total velocity curve would fall off in a manner similar to the dotted line [12].

Following Zwicky's footsteps, we can use the Virial theorem to calculate the luminous matter's contribution to the total mass of the Coma Cluster. The theorem states that for a system of N particles the time averaged total kinetic energy can be related to the time averaged total potential energy by

$$\frac{1}{2}\sum_{i=1}^{N}\langle m_i v_i^2\rangle = -\frac{1}{2}\sum_{i=1}^{N}\langle \mathbf{r}_i \cdot \mathbf{F}_i\rangle \tag{1}$$

where m_i,v_i, and $\mathbf{r}_i$ are the mass, velocity, and position of the ith particle with respect to the center of mass in a system of particles, and $\mathbf{F}_i$ is the force acting on the same particle. Since the total force on a particle is the sum of all of the forces acting on it

$$\mathbf{F}_i = \sum_{j=1}^{N}\mathbf{F}_{ji} \tag{2}$$

where $\mathbf{F}_{ji}$ is the force that particle j applies on particle i. Noting that a particle does not apply force to itself, and that Newton's third law of motion states that $\mathbf{F}_{ji} = -\mathbf{F}_{ij}$ we can rewrite the right hand side of the Virial theorem to be

$$\sum_{i=1}^{N}\mathbf{F}_i \cdot \mathbf{r}_i = \sum_{i=1}^{N}\sum_{j<i}\mathbf{F}_{ji} \cdot \mathbf{r}_i + \sum_{i=1}^{N}\sum_{j>i}\mathbf{F}_{ji} \cdot \mathbf{r}_i = \sum_{i=1}^{N}\sum_{j<i}\mathbf{F}_{ji} \cdot (\mathbf{r}_i - \mathbf{r}_j). \tag{3}$$

Using the law of gravitation to apply equation 3 to a cluster of galaxies, the Virial theorem becomes

$$\sum_{i=1}^{N}\langle m_i v_i^2\rangle = \sum_{i}^{N}\sum_{j<i}\left\langle \frac{G m_i m_j}{r_{ij}}\right\rangle \tag{4}$$

where G is the gravitational constant. The left hand side of this equation is the total mass, M, of the cluster of galaxies multiplied by the time and mass averaged squared velocity. The right hand side is approximately equal to $\frac{GM^2}{R}$, where R is the radius of the galaxy cluster. Rearranging equation 4, we arrive at an equation which relates the total mass of the galaxy cluster to the mean square velocity

$$M \approx \frac{\langle v^2 \rangle R}{G} \tag{5}$$

The mean square velocity of a galaxy cluster can be estimated by calculating the one dimensional line of sight velocity via redshift. Under the assumption of spherical symmetry

$$\langle v^2 \rangle = 3\langle (v_r - c\langle z \rangle)^2 \rangle \tag{6}$$

where $\langle z \rangle$ is the average redshift of the galaxy cluster, v_r is the line of sight velocity, and c is the speed of light. For the Coma cluster $\langle z \rangle = 0.0232$, which produces an estimate of $\langle v^2 \rangle \approx 6 \times 10^{12}$ m^2/s^2 [49]. Using the measured half-light radius of the Coma cluster ($R \approx 5 \times 10^{22}$ m) the total mass of the system in terms of solar mass ($M_\odot$) is found to be

$$M_{total} \approx 2 \times 10^{15} M_\odot. \tag{7}$$

It is is also possible to measure the mass of a galaxy cluster from luminous matter alone. The luminosity density of the universe around 445 nm has been observed to be

$$j = 1.0 \times 10^8 e^{\pm 0.26} h L_\odot \mathrm{Mpc}^{-3}, \tag{8}$$

where $h = H_0/100$ is in the dimensionless units of 100 km/s/Mpc, H_0 is Hubble's constant, and $L_\odot$ is the luminosity of the Sun in the B band. The critical mass density of the universe is given by

$$\rho_c = \frac{3H_0^2}{8\pi G} = 1.88 \times 10^{-29} h^2 \mathrm{g\ cm}^2, \tag{9}$$

where G is the gravitational consant. The ratio of these two quantities defines the mass-to-light ratio,

$$\Gamma = 2800 e^{\pm 0.3} h \frac{M_\odot}{L_\odot} \tag{10}$$

which can be used to convert the luminosity of a galaxy cluster to an estimate of the mass contributed by luminous matter alone [31].

Comparing the mass calculated from the virial theorem to the mass measured from luminosity observations of the Coma cluster we see that the luminous components contribute only a small fraction of the total mass of the system [49].

$$\frac{M_{lum}}{M_{total}} \approx \frac{2.3 \times 10^{14} M_\odot}{2 \times 10^{15} M_\odot} = 0.11 \tag{11}$$

1.1.2 Mass Measurements from x-ray Gases

Measuring the density profile of x-ray gases provides another technique to measure the total mass of a galaxy cluster. The total mass of a dynamically relaxed galaxy cluster can be measured from the hydrostatic equilibrium equation, which can be derived from the Tolman-Oppenheimer-Volkoff equation for stellar structure by taking the nonrelativistic limit of $c \to \infty$, such that

$$\frac{dP}{dr} = -\frac{GM(r)}{r^2} \rho \tag{12}$$

where P is the pressure of the gas in a cluster, G is the gravitational constant, $M(r)$ is the mass of the galaxy cluster within a particular radius, and ρ is the density of the gas in the cluster [58]. From the ideal gas law we know that

$$P = \left(\frac{\rho}{\mu m_H} \right) kT \tag{13}$$

where μ is the mean molecular weight ($\sim$0.6 as a fraction of the mass of a hydrogen atom for an ionized plasma [14]), m_H is the mass of the hydrogen atom, and k is Boltzman's constant. Plugging this into equation 12 yields

$$\frac{k}{\mu m_H}\left(T\frac{d\rho}{dr}+\rho\frac{dT}{dr}\right)=-\frac{GM(r)}{r^2}\rho \tag{14}$$

Solving equation 14 for $M(r)$ produces a measurement of the cluster's mass from x-ray gas density and temperatures

$$M(r)=-\frac{kT}{\mu m_H G}\left(\frac{d\ \ln(\rho)}{d\ \ln(r)}+\frac{d\ \ln(T)}{d\ \ln(r)}\right)r \tag{15}$$

where the logarithms were introduced using the fact that

$$\frac{r}{T}\frac{dT}{dr}=\frac{\frac{dT}{T}}{\frac{dr}{r}}=\frac{d\ \ln T}{d\ \ln r}. \tag{16}$$

This mass measurement technique is complicated by the fact that the gas density and temperature of a galaxy cluster has spatial variation, as well as the fact that x-ray emission measurements are a two-dimensional projection of a three-dimensional object, which produces complications when integrating x-ray spectra along lines of sight through the cluster. One method for simplifying the mass measurement, called the beta model, is to assume the cluster is made of isothermal, spherically symmetric gas. In this case the density of the gas traces the density of the gravitational mass, such that

$$\rho_{gas}(r)=\rho_0\left(1+\frac{r}{r_c}\right)^{-3\beta/2} \tag{17}$$

where r_c is the core radius, ρ_0 is the central density, and β is a slope parameter [56]. The core radius r_c is defined using the intensity of x-ray observations such that $I(r_c) = \frac{1}{2}I(0)$, or more generally to be the radius at which $\frac{d^2 \ln(I)}{d \ln(r)^2}$ is maximized. In this model the mass measurement reduces to a derivation of the spatial density profile by determining the best fit parameters of r_c and β to the x-ray observations. When this mass measurement technique is compared to mass measurements from luminous matter alone more evidence for dark matter arises. For example, using this technique the Virgo Cluster has been measured to have a total mass (within r < 1.8Mpc) between $1.5 \times 10^{14} M_\odot$ and $5.5 \times 10^{14} M_\odot$ [55]. Comparing this to the mass measured from x-ray luminosity yields a ratio of

$$\frac{M_{lum}}{M_{total}} \approx \frac{4.75 \times 10^{13} M_\odot}{3.5 \times 10^{14} M_\odot} = 0.14 \tag{18}$$

1.1.3 Gravitational Lensing

Gravitational lensing provides an independent method for measuring the mass of galaxy clusters and other astronomical objects. Gravitational lensing can be divided into two categories – strong lensing and weak lensing. Strong lensing, in which a background light source is distorted into arcs around a massive foreground object, is a rare phenomenon which requires a light source and a very massive lens to be nearly in line with the observer. When such a situation occurs the mass of the lens can be inferred from the angular width of the arc of light which is produced. We turn to general relativity to derive the equation which produces this mass measurement.

The geodesic equation, which describes the path that a free particle travels, is given by

$$\frac{d}{d\tau}\left(g_{aj}\frac{dx^j}{d\tau}\right) - \frac{1}{2}\frac{\partial g_{ij}}{\partial x^a}\frac{dx^i}{d\tau}\frac{dx^j}{d\tau} = 0 \tag{19}$$

where $g_{\alpha j}$ is a metric, τ is the proper time, and x is the four dimensional coordinate vector. For a spacetime in a vacuum outside of a spherically symmetric mass the appropriate metric to use is the Schwarzschild metric. With units of $c = 1$ it is given by

$$ds^2 = -\left(1 - \frac{2GM}{r}\right)dt^2 + \left(1 - \frac{2GM}{r}\right)^{-1}dr^2 + r^2 d\theta^2 + r^2 sin^2\theta d\phi^2. \tag{20}$$

From the t component of the geodesic equation we know that

$$\frac{d}{d\tau}\left(g_{tj}\frac{dx^j}{d\tau}\right) - \frac{1}{2}\frac{\partial g_{ij}}{\partial t}\frac{dx^i}{d\tau}\frac{dx^j}{d\tau} = 0. \tag{21}$$

The Schwarzschild metric does not depend on time, and is diagonal, therefore

$$\frac{d}{d\tau}\left(g_{tj}\frac{dx^j}{d\tau}\right) = \frac{d}{d\tau}\left(g_{tt}\frac{dt}{d\tau}\right) = -\frac{d}{d\tau}\left(\left(1 - \frac{2GM}{r}\right)\frac{dt}{d\tau}\right) = 0. \tag{22}$$

Equation 22 is true if the quantity inside of the derivative is constant, leading us to the first constant of motion

$$E = \left(1 - \frac{2GM}{r}\right)\frac{dt}{d\tau}. \tag{23}$$

We now turn to the ϕ component of the geodesic equation

$$\frac{d}{d\tau}\left(g_{\phi j}\frac{dx^j}{d\tau}\right) = \frac{d}{d\tau}\left(g_{\phi\phi}\frac{d\phi}{d\tau}\right) = -\frac{d}{d\tau}\left(r^2 sin^2\theta\frac{d\phi}{d\tau}\right) = 0 \tag{24}$$

where we have once again used the fact that the metric does not depend on time and is diagonal to simplify the equation. From this we arrive at the second constant of motion

$$l = r^2 sin^2\theta \frac{d\phi}{d\tau} \tag{25}$$

Returning to the Schwarzschild metric, for a photon $ds^2=0$, and if we assume motion in the equatorial plane $\theta = \pi/2$ and $d\theta = 0$, such that

$$-\left(1 - \frac{2GM}{r}\right) dt^2 + \left(1 - \frac{2GM}{r}\right)^{-1} dr^2 + r^2 d\phi^2 = 0. \tag{26}$$

From the two constants of motion we know that

$$d\phi^2 = \frac{l^2}{r^4 sin^4\theta} d\tau^2 \tag{27}$$

and

$$dt^2 = E^2 \left(1 - \frac{2GM}{r}\right)^{-2} d\tau^2 \tag{28}$$

Plugging equations 27 and 28 into equation 26 and simplifying yields

$$dr^2 = \left[E^2 - \left(1 - \frac{2GM}{r}\right) \frac{l^2}{r^2}\right] d\tau^2 \tag{29}$$

Finally, by dividing equation 29 by equation 27 we arrive at the equation of motion for light traveling in a Schwarzschild spacetime in polar coordinates

$$\left(\frac{1}{r^2}\frac{dr}{d\phi}\right)^2 = \left(\frac{E}{l}\right)^2 - \left(1 - \frac{2GM}{r}\right)\frac{1}{r^2} \equiv \left(\frac{1}{b}\right)^2 - \left(1 - \frac{2GM}{r}\right)\frac{1}{r^2} \tag{30}$$

The quantity $b \equiv l/E$ is known as the impact parameter, which represents the perpendicular distance between the center of attraction and the particle's initial trajectory. To determine the change in the direction of light due to a gravitational field we must integrate $\frac{d\phi}{dr}dr$ from the minimum distance the light travels by the massive object, denoted as R, and then multiply by a factor of 2 to account for the symmetrical motion of the particle during its approach to the object. Note that at a distance R the light is moving tagentially, such that $\frac{dr}{dt} = 0$ and equation 30 becomes

$$\frac{1}{b^2} = \left(1 - \frac{2GM}{R}\right)\frac{1}{R^2}. \tag{31}$$

Therefore, we can rewrite equation 30 for any value of r as

$$\left(\frac{1}{r^2}\frac{dr}{d\phi}\right)^2 = \left(1 - \frac{2GM}{R}\right)\frac{1}{R^2} - \left(1 - \frac{2GM}{r}\right)\frac{1}{r^2}. \tag{32}$$

Making the convenient substitution of $u \equiv R/r$, where $0 \leq u \leq 1$ in equation 32 yields

$$\left(\frac{du}{d\phi}\right)^2 = 1 - u^2 - \frac{2GM}{r}(1 - u^3). \tag{33}$$

From this we can find an equation for the infinitesimal variation $d\phi$ in terms of du

$$d\phi = \frac{(1-u^2)^{-1/2}du}{\left[1 - \frac{2GM}{R}(1-u^3)(1-u^2)^{-1}\right]^{-1/2}}. \tag{34}$$

A further substitution of $u \equiv \cos(\alpha)$, where $0 \leq \alpha \leq \pi/2$, leads (after some simplification) to the equation

$$d\phi = \left[1 - \frac{2GM}{R}\left(\cos(\alpha) + \frac{1}{1+\cos(\alpha)}\right)\right]^{-1/2} d\alpha. \tag{35}$$

In most cases, the quantity $M/R << 1$, so we can use the approximation $(1+x)^n \approx 1+nx$ for small x in equation 35 such that

$$d\phi = \left[1 + \frac{GM}{R}\left(\cos(\alpha) + \frac{1}{1+\cos(\alpha)}\right)\right] d\alpha. \tag{36}$$

This is known as the "weak field" limit. Integrating this expression from $0 \leq \alpha \leq \pi/2$ and multiplying by 2 to account for the two symmetrical legs of the light's trajectory provides an expression for the total azimuthal angle of the light.

$$\phi = 2\int_0^{\pi/2} \left[1 + \frac{GM}{R}\left(\cos(\alpha) + \frac{1}{1+\cos(\alpha)}\right)\right] d\alpha = \pi + \frac{4GM}{R}. \tag{37}$$

Noting that the first term, π, is the azimuthal angle of the light if no mass were present, we arrive at an equation that relates the angle of deflection of light to the total mass of the gravitational object.

$$\Delta\phi = \phi - \pi = \frac{4GM}{R}. \tag{38}$$

In practice, we must go one step further to turn astronomical observations of gravitational lensing into a mass measurement. Any observation of a lensed light source involves an observer viewing an image of the object after it passes by a gravitational lens. This situation is depicted in Figure 2. To measure the mass of a lens we seek to relate the source position to the image position. Using the small angle approximation for θ and β we can arrive at

$$D_S\theta = D_S\beta + D_{LS}\Delta\phi. \tag{39}$$

where $D_s = D_L + D_{LS}$ is the distance from the source plane to the observer. Using equation 38, and the fact that $R \approx \theta D_L$ this becomes

$$\theta = \beta + \frac{4GMD_{LS}}{\theta D_L D_S} \tag{40}$$

This is a quadratic equation with roots

$$\theta = \frac{\beta \pm \sqrt{\beta^2 + 4\theta_E^2}}{2} \tag{41}$$

where $\theta_E = \left(4GM\frac{D_{LS}}{D_S D_L}\right)^{1/2}$ is the angular size of the "Einstein ring" that forms when the source and lens are perfectly aligned. If the quantities D_{LS}, D_L, and β are known, equation 41 can be used to measuring the mass of the lens by measure the angle of deflection θ [16]. In the handful of cases in which this mass measurement has been carried out, it has been found to be consistent with dark matter models [57].

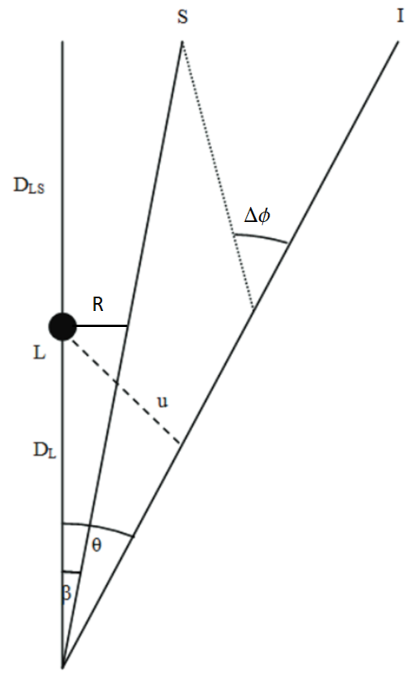

Figure 2: A source emits light at position S. The light is deflected by a massive lens at L, and causes the image seen by the observer to appear at an angle θ. D_{LS}, D_L, θ, and β are, respectively, the distance from the lens plane to the source plane, the distance from the lens plane to the observer, the angle of the image relative to the observer, and the angle of the source relative to the observer [16].

Although there are only a few cases in which strong gravitational lensing can be observed, there are numerous cases of weak gravitational lensing. Weak lensing occurs when the lensing mass isn't large enough for strong lensing, or if the source of light is not directly aligned with the lensing mass, resulting in a shear distortion of the image. Measuring the mass of a weak lens is complicated by the fact that each light source has a unique, intrinsic ellipticity which typically dwarfs the magnitude of the image distortion. This intrinsic ellipticity is known as "shape noise" in weak gravitational lensing studies. In cases where many sources are lensed by the same object, the distortion from the lens can be measured by averaging over the many source images, taking advantage of their random intrinsic orientation.

In these cases, the measured shear distortion results from photons being deflected by mass fluctuations along the line of sight. In this case, the two dimensional lens equation (analogous to equation 40) in vector format is

$$\boldsymbol{\beta} = \boldsymbol{\theta} - \frac{D_{LS}}{D_S}\Delta\boldsymbol{\phi}(\boldsymbol{\xi}) \tag{42}$$

where $\boldsymbol{\xi} = D_S\boldsymbol{\theta}$ is the impact parameter. The deflection angle can be calculated by integrating the 3D gravitational potential, $\boldsymbol{\Phi}(\mathbf{r})$, along the line of sight such that

$$\Delta\boldsymbol{\phi}(\boldsymbol{\xi}) = 2\int \nabla_{\perp}\boldsymbol{\Phi}(\mathbf{r})dz = \nabla_{\perp}\left(2\int \boldsymbol{\Phi}(\mathbf{r})dz\right) \equiv \nabla_{\perp}V. \tag{43}$$

Assuming the angle between the image and the observer, $\boldsymbol{\theta}$, is small equation 42 can be approximated with a first order Taylor series as

$$\beta_i = A_{ij}\theta_j \tag{44}$$

where i corresponds to the i^{th} component of the lens plane, j corresponds to the j^{th} component of the source plane, and

$$A_{ij} = \frac{\partial\beta_i}{\partial\theta_j} = \delta_{ij} - \frac{\partial\Delta\phi_i(\boldsymbol{\theta})}{\partial\theta_j} = \delta_{ij} - \frac{\partial^2 V(\boldsymbol{\theta})}{\partial\theta_i\partial\theta_j} \tag{45}$$

are the elements of a Jacobian distortion matrix, $\mathbf{A}$, which describes the isotropic dilation and anisotropic distortion due to convergence and shear effects. The distortion matrix can be written in terms of the convergence, κ, which increases the size of the image while conserving brightness, and the shear, γ, which distorts the the image tangentially around the lens.

$$A_{ij} = (1-\kappa)\begin{pmatrix} 1 & 0 \\ 0 & 1 \end{pmatrix} - \gamma \begin{pmatrix} \cos(2\phi) & \sin(2\phi) \\ \sin(2\phi) & -\cos(2\phi) \end{pmatrix} \tag{46}$$

Equations 45 and 46 offer a relationship between the observable quantities κ and γ, and the gravitational potential V.

$$\gamma_1 \equiv \gamma cos 2\phi = \frac{1}{2}\left[\frac{\partial^2 V(\boldsymbol{\theta})}{\partial \theta_1^2} - \frac{\partial^2 V(\boldsymbol{\theta})}{\partial \theta_2^2}\right] \tag{47}$$

$$\gamma_2 \equiv \gamma \sin(2\phi) = \frac{\partial^2 V(\boldsymbol{\theta})}{\partial \theta_1 \partial \theta_2} \tag{48}$$

$$\kappa = \frac{1}{2}\nabla^2 V(\boldsymbol{\theta}) \tag{49}$$

where equation 47 comes from $A_{11} - A_{22}$, equation 48 comes from $A_{12} - A_{21}$, and equation 49 comes from $tr(A)$. Since κ is equal to half the laplacian of the projected gravitational potential, V, it is directly proportional to the mass density of the lens. The shear component γ_1 corresponds to elongation and compression along the x and y directions, and the component γ_2 describes elongation and compression along the diagonal $x = y$ and $x = -y$ directions. In the case of weak lensing, the mass measurement then reduces to a measurement of the shear and convergence produced by the lens [45]. As with strong gravitational lensing, weak gravitational lensing mass measurements have been found to be consistent with dark matter models [57].

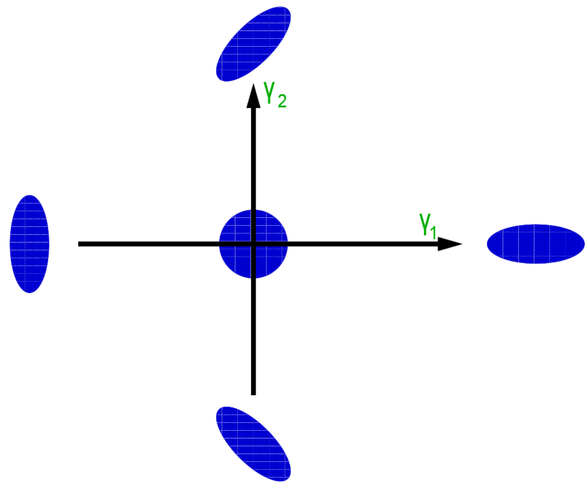

Figure 3: An illustration of how positive and negative γ_1 and γ_2 distort an object with initial ellipticity of zero [46].

One of the most famous instances of weak lensing evidence for dark matter is a collision of two galaxies clusters known as the Bullet Cluster. The baryonic matter in each galaxy cluster is predominantly in the form of hot gas. Electromagnetic interaction causes the gas to to slow down and concentrate in the center of the collision. In the absence of dark matter, gravitational lensing measurements should be correlated with the hot gas, since it is the dominant luminous mass in the system. However, if dark matter was a dominant mass component in the Bullet Cluster it would not be slowed by electromagnetic interactions and would pass through the collision without significant perturbation. Indeed, weak gravitational lensing observations show that the majority of the mass in the Bullet Cluster passed through the collision rather than concentrating at the center like the luminous matter, suggesting that dark matter is present in abundance over the baryonic matter of the two galaxy clusters [21].

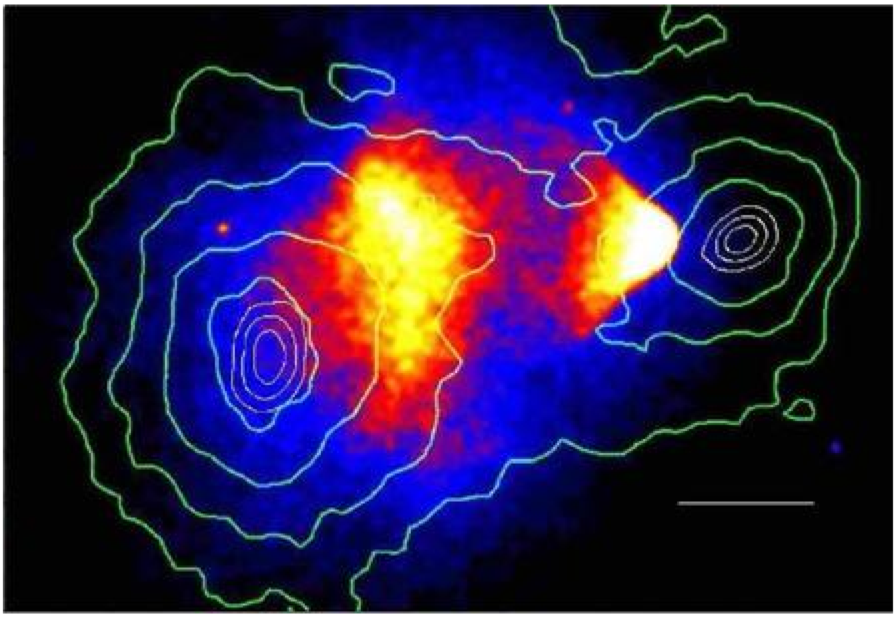

Figure 4: X-ray image of the baryonic mass in the Bullet cluster, overlayed with mass contours derived from weak lensing measurements. The separation of the dominant mass component from the baryonic matter indicates the presence of dark matter [21].

1.1.4 Cosmological Evidence

The early universe was filled with a hot, dense plasma of electrons and baryons. At this time photons scattered off of the free electrons, restricting their movement across the universe. As the universe cooled below the binding energy of hydrogen (13.6 eV) protons and electrons began to combine, forming neutral hydrogen atoms. At this point in time, known as the recombination epoch, photons and electrons decoupled and the photons began traveling with a mean free path the size of the universe. These photons produce the Cosmic Microwave Background (CMB) that we see today (Figure 5). The radiation is extremely isotropic and exhibits a black-body spectrum at a red shifted temperature of 2.72 K. The frequency spectrum, temperature fluctuations, and polarization of the CMB all contain a vast amount of information about the formation of the universe. Here, we focus on just one of these properties.

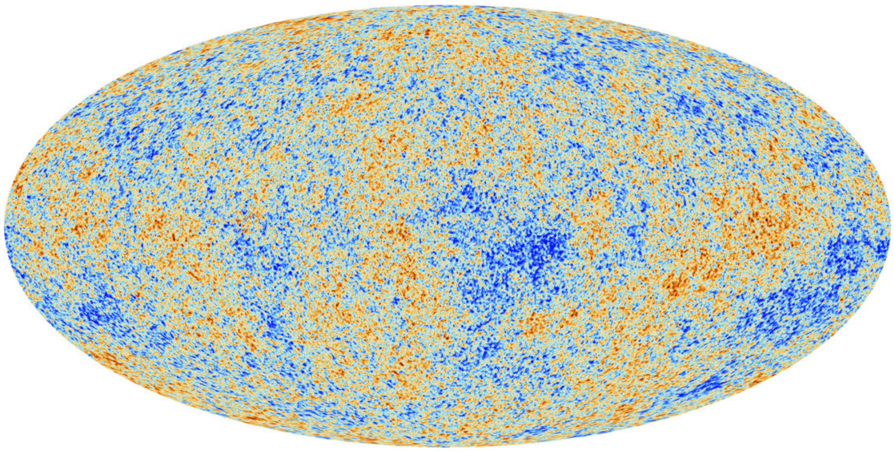

Figure 5: The latest measurement of the CMB temperature anistropies from Planck data [23].

In 1990 the COBE satellite observed small (1 part in 10,000) fluctuations in the average temperature of the CMB. Since then, the result has been confirmed by numerous ground based telescopes, as well as the WMAP and Planck satellites. We see these temperature fluctuations projected on a 2D spherical surface, so it is typical to expand them in terms of spherical harmonics defined by

$$Y_{lm} = \sqrt{\frac{2l+1}{4\pi}\frac{(l-m)!}{(l+m)!}}P_l^m(\cos\theta)e^{im\phi} \tag{50}$$

where $l = 0, ..., \infty$, $-l \leq m \leq l$, and P_l^m are associated Legendre polynomials. The temperature fluctuations can then be written as

$$f(\theta,\phi) \equiv \frac{\delta T(\theta,\phi)}{T_0} = \sum_{l=0}^{l=\infty}\sum_{m=-l}^{m=l} a_{lm}Y_{lm}(\theta,\phi) \tag{51}$$

where T_0 is the average temperature of the CMB and a_{lm} are the coefficients of expansion. Since the spherical harmonics are orthonormal

$$a_{lm} = \int_{\theta=-\pi}^{\pi} \int_{\phi=0}^{2\pi} f(\theta, \phi) Y_{lm}^*(\theta, \phi) d\Omega. \tag{52}$$

The a_{lm} coefficients represent a deviation from the average temperature T_0, so their ensemble average is zero

$$\langle a_{lm} \rangle = 0 \tag{53}$$

and their variance, $\langle |a_{lm}|^2 \rangle$, gives a measure of the typical size of a_{lm}. The temperature fluctuations are isotropic and therefore independent of m, so

$$\left\langle |a_{lm}|^2 \right\rangle = \frac{1}{2l+1} \sum_m \left\langle |a_{lm}^2| \right\rangle \equiv C_l. \tag{54}$$

where the function C_l is referred to as the angular power spectrum of the temperature fluctuations. The angular power spectrum is related to contribution of the multipole l to the temperature variance by

$$\begin{aligned} \left\langle \left(\frac{\delta T(\theta, \phi)}{T_0} \right)^2 \right\rangle &= \left\langle \sum_{lm} a_{lm} Y_{lm}(\theta, \phi) \sum_{l'm'} a_{l'm'}^* Y_{l'm'}^*(\theta, \phi) \right\rangle \\ &= \sum_{ll'} \sum_{mm'} Y_{lm}(\theta, \phi) Y_{l'm'}^*(\theta, \phi) \left\langle a_{lm} a_{l'm'}^* \right\rangle \\ &= \sum_l C_l \sum_m |Y_{lm}(\theta, \phi)|^2 = \sum_l \frac{2l+1}{4\pi} C_l \end{aligned} \tag{55}$$

where we have used the the closure relation

$$\sum_m |Y_{lm}(\theta, \phi)|^2 = \frac{2l+1}{4\pi} \tag{56}$$

and the fact that

$$\langle a_{lm} a^*_{l'm'} \rangle = \delta_{ll'} \delta mm' \left\langle |a_{lm}|^2 \right\rangle \tag{57}$$

since the a_{lm} coefficients are independent random variables [39].

Cosmological models predict the variance of the a_{lm} expansion coefficients, and therefore predict the angular power spectrum and the contribution of each multipole to the temperature variance. By measuring the angular power spectrum of the CMB and comparing to the C_l values predicted by each model we can learn about the composition of the universe. The temperature fluctuations of the CMB are typically plotted in terms of $D_l \equiv l(l+1)C_l/(2\pi)$ with units of $\mu\mathrm{K}^2$ versus the multipoles l as shown in Figure 6.

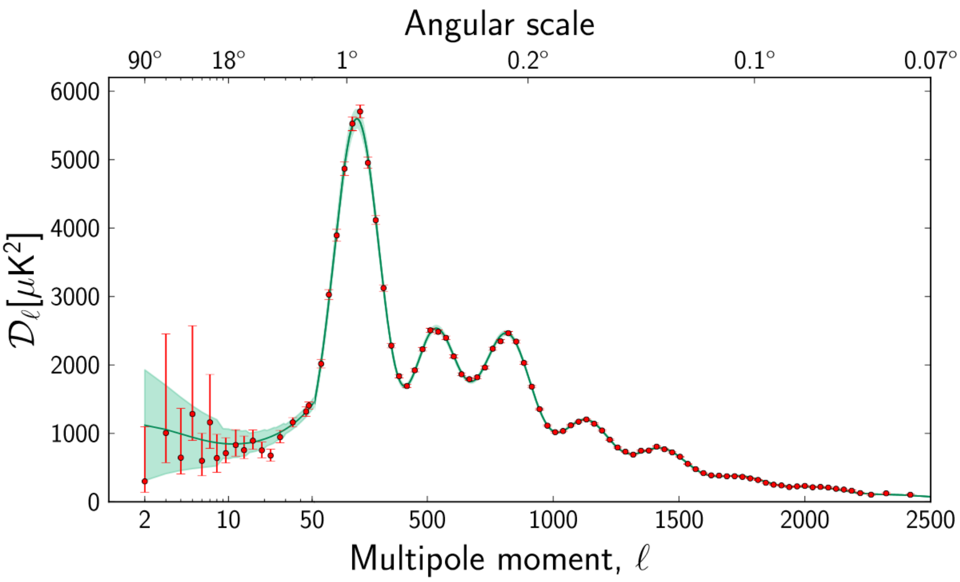

Figure 6: The power spectrum of temperature fluctuations from the CMB based on data from Planck [23].

To understand the wealth of information present in Figure 6 we must first understand the origin of the temperature fluctuations in the early universe. Prior to recombination the primordial plasma consisted of anistropic regions of varying density. Overdense regions of matter would gravitationally attract more matter. As this happened, heat from photons scattering off of free electrons would produce an increase in pressure, counteracting the force of gravity and pushing baryonic matter away from the high density regions. As these two processes competed they produced oscillations in the distribution of baryonic matter, which we refer to as Baryon acoustic oscillations (BAO). After recombination the photons diffused through the baryonic matter, removing the source of pressure, ending the oscillating process, and leaving a shell of overdense baryonic matter at the origin of the anisotropy and at a fixed radius called the sound horizon.

The first peak in Figure 6 details the curvature of the universe. If the universe had positive curvature the light from the CMB would be magnified, shifting the first peak to lower multipole in Figure 6. Likewise, in a negatively curved universe the scale of the temperature fluctuations in the CMB would appear diminished, shifting the first peak to higher multipole. The observed location of the first peak, close to $l \sim 200$, turns out to be consistent with a flat universe.

The second peak in Figure 6 details the amount of baryonic matter in the universe. Baryons add mass to the system during the oscillating process described above. This additonal inertia forces the primordial plasma to travel farther before recoiling back to the center of the anistropy, much like adding a mass to the end of a spring. The odd numbered peaks in Figure 6 are associated with how far the plasma compresses during BAO and are enhanced by the presence of additional baryons, as shown in Figure 7. The even numbered peaks are associated with how far the plasma rebounds during BAO and are unaffected by the presence of additional baryons. Therefore, the presence of baryons enhances the size of the odd peaks over the even peaks such that a smaller second peak in Figure 6 corresponds to a larger amount of baryonic matter in the universe. The latest results from Planck indicate that baryonic matter makes up $4.82 \pm 0.05\%$ of the universe.

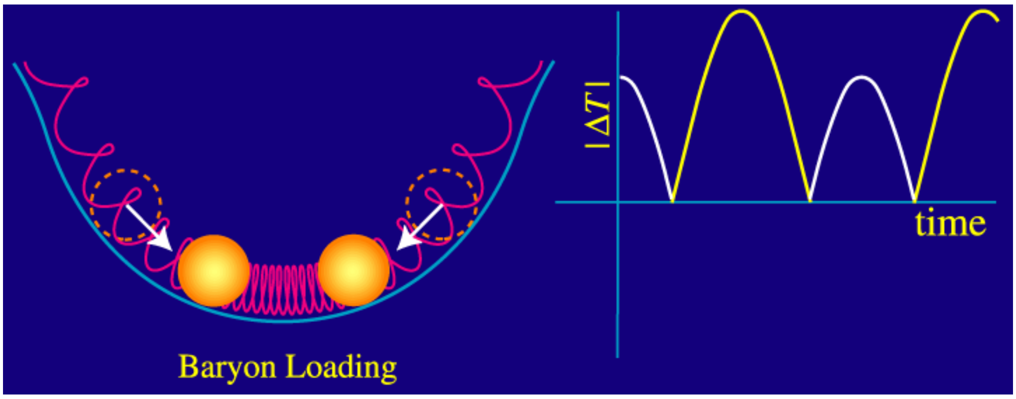

Figure 7: A depiction of the effect of baryons on the oscillating plasma during BAO. The mass of the baryons loads down the plasma, producing an asymmetry in the oscillations in which the plasma compresses further toward the minimum of the potential well. Since the CMB power spectrum does not care about the sign of the fluctuation, we see that the odd numbered peaks become enhanced over the even numbered peaks [33].

The third peak in Figure 6 details the amount of dark matter in the universe. Since the very early universe was dominated by photon-baryon interactions, the outward pressure caused the gravitational potential of the BAO system to decay in such a way that it drove the amplitude of oscillations higher. With higher dark matter density this driving effect is diminished (since dark matter does not rebound) and the overall magnitude of the peaks becomes smaller. Although this effects all of the peaks in Figure 6 it is only distinguishable in the third peak. Furthermore, as with ordinary matter, dark matter was gravitationally attracted to areas with higher density. Since dark matter does not interact through the electromagnetic force it was unaffected by the increasing photon pressure which produced acoustic oscillations in baryons. As a result, a higher density of dark matter corresponded to a larger gravitational potential well for baryons to fall into during their oscillations, increasing the amplification of BAO on the odd numbered peaks. Therefore, the height of the third peak tells us the amount of dark matter that is present in the universe [33]. The Planck observations indicates that dark matter makes up $25.8 \pm 0.4\%$ of the universe. The remaining $69.4 \pm 1.0\%$ of the universe is made up of dark energy [23].

1.2 Dark Matter Candidates

1.2.1 The ΛCDM Model

To further examine the properties of dark matter it is useful to introduce a quantitative measure for the composition of the universe. Friedmann's equation, which describes the expansion of space in a homogeneous and isotropic universe, is given by

$$\frac{\dot{a}^2 + kc^2}{a^2} = \frac{8\pi G\rho + \Lambda c^2}{3}, \tag{58}$$

where a is the scale factor of the universe, k is the spatial curvature of the universe (equivalent to one sixth of the Ricci Scalar) , c is the speed of light, G is the gravitational constant, ρ is the density of the universe, and Λ is the cosmological constant. Einstein's field equations,

$$G_{\mu\nu} = \frac{8\pi G}{c^4} T_{\mu\nu} \tag{59}$$

provide an expression for the cosmological constant, Λ. We can split the stress energy tensor into two terms, one describing matter and the other describing the vacuum, such that $T_{\mu\nu} = T_{\mu\nu}^{matter} + T_{\mu\nu}^{vac}$. Since the stress energy tensor is given by

$$T_{\mu\nu} = (\rho + p)U_\mu U_\nu + p g_{\mu\nu}, \tag{60}$$

and to maintain Lorentz invariance $p^{vac} = -\rho^{vac}$, we can write the vacuum component of the stress energy tensor as

$$T_{\mu\nu}^{vac} = -\rho^{vac} g_{\mu\nu}. \tag{61}$$

If we identify the vacuum energy density as

$$\rho^{vac} = \frac{\Lambda c^2}{8\pi G} \tag{62}$$

then Einstein's field equation takes on the familiar form

$$G_{\mu\nu} + g_{\mu\nu}\Lambda = \frac{8\pi G}{c^4} T_{\mu\nu}^{matter}, \tag{63}$$

where $G_{\mu\nu}$ is the Einstein tensor, $g_{\mu\nu}$ is the metric tensor, G is the gravitational constant, and Λ is the cosmological constant. Setting the normalized spatial curvature $k = 0$ in Friedmann's equation(representing a flat universe), one can find the critical density for which the universe is spatially flat to be

$$\rho_c = \frac{3}{8\pi G}\frac{\dot{a}^2}{a^2}, \tag{64}$$

where $\rho_c = \rho^{vac} + \rho$. Recognizing Hubble's constant to be $H_0 = \frac{\dot{a}}{a}$, we can rewrite this as

$$\rho_c = \frac{3H_0^2}{8\pi G} \tag{65}$$

where H_0 is the present value of the Hubble constant [34]. The current experimental value for H_0 in the dimensionless units 100 km/s/Mpc is $h \sim 0.7$ with an uncertainty of $\sim 5\%$ [25]. We can then define the density parameter as

$$\Omega = \frac{\rho}{\rho_c} = \frac{8\pi G\rho}{3H_0^2}. \tag{66}$$

If Ω is larger than unity the universe is spatially closed, and if Ω is less than unity the universe is spatially open. This density parameter can be split into components, such that for a particular component x

$$\Omega_x = \frac{\rho_x}{\rho_c}. \tag{67}$$

Detailed cosmological studies have concluded that all the luminous matter in the universe has a density parameter of $\Omega_{lum} \lesssim 0.01$. This information, combined with the fact that analysis of galactic rotational velocities implies >90% of the mass in galaxies is dark leads to the conclusion that $\Omega_{DM} \geq 0.09$. This is only a lower limit on the dark matter density parameter, since most rotation curves remain flat out to the largest radii at which they can be measured and it can be assumed that the DM halos extend even farther out.

It is possible that baryonic DM alone could be responsible for the dark matter halos. However, other analyses eliminate this possibility. Direct searches for massive compact halo objects (MACHOs) utilizing microlensing have determined that $<25\%$ of the dark halos could be due to baryonic dark matter within the mass range of $2 \times 10^{-7} M_{\odot} < M < 1 M_{\odot}$ at a 95% confidence limit [8, 10]. Furthermore, data from the Hubble Deep Field Space Telescope suggests dark matter halos consist of $\leq 5\%$ white dwarfs [28].

With baryonic dark matter being ruled out as the sole component of dark matter halos we now investigate the other density parameter components. Big Bang nucleosynthesis models constrain the amount of baryonic matter in the universe to $\Omega_b \approx 0.045$ (where b stands for baryons) [54]. Additionally, analysis of velocity flows, x-ray emissions temperatures, and gravitational lensing in large clusters and superclusters of galaxies suggests that the total matter component of the universe has density parameter $\Omega_m \approx 0.2 - 0.3$. One can combine this information, assuming $h = 0.7$ to find density parameters that are consistent with the Planck observation of

$$\Omega_b = 4.82 \pm 0.05\%$$

$$\Omega_{nbm} = 25.8 \pm 0.4\%$$

$$\Omega_{\Lambda} = 69.4 \pm 1.0\%$$

where Ω_b is the baryonic density of the universe, Ω_{nbm} is the nonbaryonic density parameter of the universe, and Ω_{Λ} is the dark energy density parameter of the universe [52, 23]. This is known as the Λ-CDM model.

1.2.2 Nonbaryonic Dark Matter

With $\Omega_{nbm} = 25.8 \pm 0.4\%$ it is intriguing to look at the particles which have been proposed to explain this contribution to the total density parameter. One such particle is the standard-model neutrino. The neutrino is an electrically neutral, weakly interacting particle with a nearly zero mass. Neutrinos exist in three distinct flavors – the electron neutrino (ν_e), the muon neutrino (ν_μ), and the tau neutrino (ν_τ). It is known that neutrinos oscillate between these three flavors, with each flavor state being a superposition of three neutrino states of definite mass (ν_1,ν_2, and ν_3). Experiments studying solar neutrino oscillations have determined the squared mass difference between what is known as the solar neutrino doublet (ν_1 and ν_2) to be $\delta m^2 = (7.66 \pm 0.35) \times 10^{-5}$ eV^2, while experiments studying atmospheric neutrino oscillations have determined the remaining squared mass difference between the solar neutrino doublet and ν_3 to be $\pm(2.38 \pm 0.27) \times 10^{-3}$ eV^2 up to an unknown sign [47]. This sign ambiguity leads to two possible hierarchies for the neutrino mass states. (Figure 8) In either case, we can set a lower limit on the most massive neutrino state to be $m_{\nu_3} \gtrsim 0.05$ eV.

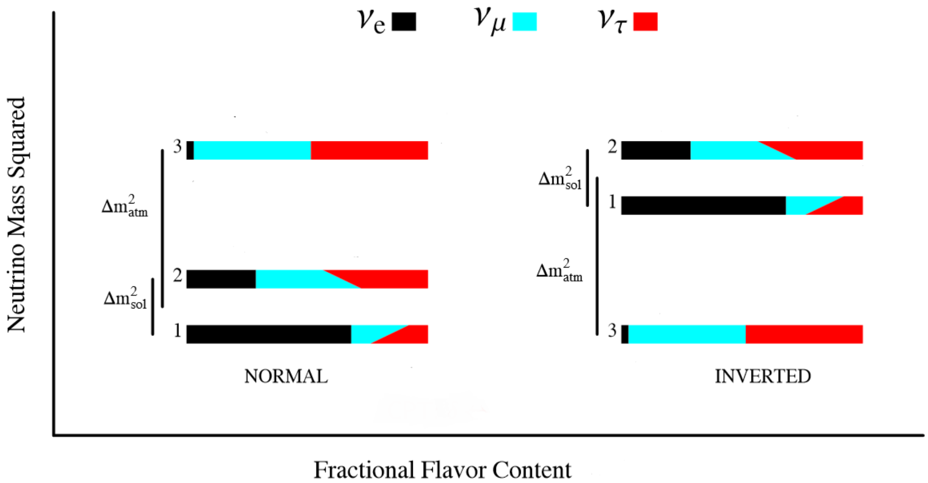

Figure 8: The two hierarchies of neutrino mass states. Black, teal, and red indicated the three flavors of neutrinos, while one, two, and three indicated the three mass states [41].

The density parameter of neutrinos is given by

$$\Omega_\nu = \frac{\rho_\nu}{\rho_c} = \frac{1}{h^2}\sum_{i=1}^{3}\frac{g_i m_i}{90\ \mathrm{eV}},$$

where $g_i = 1$ for Majorana neutrinos (own antiparticle) and $g_i = 2$ for Dirac neutrinos (distinct antiparticles) [42]. Using the lower mass limit of the neutrino and assuming Majorana neutrinos, this suggests a lower limit on the neutrino density parameter of $\Omega_\nu \gtrsim 0.00122$. Thus, neutrinos do provide some contribution to the nonbaryonic dark matter density parameter.

To find an upper limit on the neutrino contribution to the nonbaryonic dark matter density parameter is is necessary to distinguish hot dark matter from cold dark matter. Hot dark matter is composed of particles that have zero or nearly-zero mass. Special relativity requires that the massless particles move at the speed of light, and that the nearly-massless particles move close to the speed of light if they have any substantial momentum. As a result hot dark matter forms very hot gases. Cold dark matter is composed of particles that at sub-relativistic velocities. With their low masses neutrinos fall under the hot dark matter category. A combination of galaxy clustering measurements, CMB observations, and Lyman-α observations give an upper limit on the hot dark matter contribution of $\Omega_\nu \lesssim 0.0155$, thus neutrinos and other hot dark matter particles cannot be the primary contribution to the nonbaryonic dark matter density parameter [52].

1.2.3 WIMPs and SUSY

If we assume cold dark matter (CDM) particles were in thermal equilibrium with the other standard-model particles during the early stages (<1 ns) of the universe it is possible to calculate the CDM density parameter. As the temperature, T, of the universe cools, the particles with masses $m > T$ will diminish exponentially. Once the temperature of the universe cooled below the CDM mass scale the creation of these particles would have ceased. At this time the CDM particles which still existed would have continued annihilating with one another. As time went on, CDM annihilation became less and less likely due to their dwindling abundance. Once the expansion rate of the universe, given by Hubble's constant, exceeded the CDM annihilation rate, the CDM particles dropped out of thermal equilibrium and the CDM density became fixed.

The density parameter for CDM is approximately given by

$$\Omega_{CDM}h^2 \simeq \frac{T_0^3}{M_{Pl}\langle\sigma_A\nu\rangle}$$

where σ_A is the total annihilation cross section of CDM particles, ν is the relative velocity of CDM particles, T_0 is the equilibrium temperature at freeze out, M_{Pl} is the Planck mass, c is the speed of light, and $\langle ... \rangle$ represents an average over the thermal distribution of CDM particle velocities [38, 35]. Remarkably, for the total density parameter of the universe to equal unity, as required by cosmological observations, an annihilation cross section on the order of particles interacting on the electroweak scale ($\sim 10^{-9}$ GeV^{-2}) is required for CDM particles. This result is the main motivation behind suspecting weakly interacting massive particles (WIMPs) as the dominant contribution to the nonbaryonic dark matter density parameter.

Supersymmetry (SUSY) is a symmetry of space-time which has been proposed in an effort to unify the electroweak, strong, and gravitional forces. This theory offers some insight into the nature of WIMPs. SUSY requires that a supersymmetric partner particle exists for each particle in the standard model. These partners go by the names of sleptons (partners of leptons), squarks (partners of quarks), gauginos (partners of gauge bosons), and higgsinos (partners of Higgs bosons). Sleptons and squarks have spin zero, while gauginos and higgsinos have spin one-half. Since none of these supersymmetric particles have been discovered it is thought they are far more massive than their standard model counterparts, and thus that supersymmetry is not an explicit symmetry of nature.

Goldberg [30] and Ellis [27] have suggested that neutral gauginos and neutral higgsinos can mix together in a superposition known as the neutralino, χ. In most SUSY models, the neutralino is the lightest supersymmetric particle (LSP). In models which conserve R-parity (a new quantum number distinguishing SUSY particles from standard model particles) the LSP is stable, making it a prime candidate particle for dark matter. The expected cross section of neutralinos interacting via inelastic collisions with nucleons is dependent on the allowed regions of parameter space in the SUSY model being used.

The neutralino is one of many candidate particles suggested for WIMPs, and as previously mentioned, WIMPs are not the only candidate for dark matter. In the following sections we will briefly discuss some of the other candidates before returning to the discussion of WIMPs in Chapter 2.

1.2.4 Axions and Axinos

Quantum chromodynamics (QCD) is a theory describing the strong interaction between quarks and gluons, which make up hadrons. In particle physics there exists a proposed symmetry of nature referred to as charge conjugation parity symmetry (CP-Symmetry). CP-Symmetry postulates that particles should behave the same if they are replace by their own antiparticle (C symmetry), and then have their parity reversed (P symmetry). Within QCD there is no theoretical reason to assume CP-symmetry exists. However, when a CP-violation term is included in the QCD lagrangian its coefficient has been experimentally determined to be less than 10^{-10} [11]. This unexpected result is known as the strong CP problem in quantum chromodynamics. To reconcile this, a new symmetry known as the Peccei-Quinn theory has been proposed. This theory postulates the existence of a new pseudoscalar particle called the axion. According to the Peccei-Quinn theory, axions would be electrically neutral, stable, low mass (1μ eV - 1 eV) particles that have very low interaction cross sections for the strong and weak forces. Therefore, axions satisfy all of the requirements to be a dark matter candidate.

If axions exists, they would be observable through an $a \rightarrow \gamma\gamma$ interaction. Figure 9 shows limits that various axion detection experiments have placed on the effective coupling of this process. Dark matter axions would lie somewhere between the lines labeled as "KSVZ" and "DFSZ". (KSVZ and DFSZ are acronyms for two "invisible axion" theories which describe the axion as a dark matter candidate) At the top of Figure 9, axions would be observable through seismic signatures in the Sun, as well as through scattering processes in germanium crystals. These processes have not been observed, so they are used to exclude possible values of the coupling constant. In the upper right, the optical photons from axion decay in the halos around astrophysical object would be observable in telescopes. Axion emission from astrophysical objects would affect the evolution of those objects, placing an upper limit on the coupling constant at $\sim 10^{-10}$ GeV^{-1}. Axion emissions in supernovae would shorten the duration of neutrino bursts detected on Earth seen from sn1987a. These observations place the strongest upper limit on the coupling constant at $\sim 10^{-13}$ GeV^{-1}. (Not depicted in the figure) These limits produce a small window between 1-100 μeV in which axion dark-matter can exist, which the Axion Dark Matter Experiment (ADMX) experiment is currently searching [48].

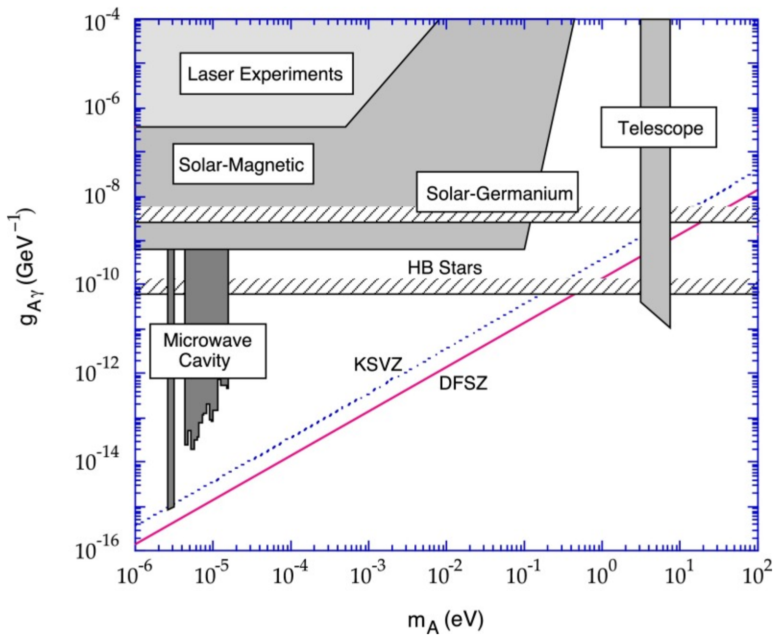

Figure 9: Historical limits placed on axion masses and photon coupling constants. If dark matter axions exist, they would lie between the lines labeled KSVZ and DFSZ [48].

1.2.5 Gravitons and Gravitinos

In quantum field theory, the graviton is a hypothetical elementary particle which mediates the gravitational force. As with axions and axinos, when SUSY is introduced to quantum field theory a supersymmetric partner to the graviton is predicted to exist known as the gravitino. In some models, gravitinos are the LSP in SUSY and are thus a candidate particle for dark matter.

1.2.6 WIMPzillas

WIMPzillas are supermassive dark matter particles which arise when one considers the possibility that dark matter might be composed of nonthermal supermassive states. These particles would have a mass many orders of magnitude higher than the weak scale [20]. Studies have shown that for stable particles with masses close to 10^{13} GeV WIMPzillas would be produced in sufficient abundance to give $\Omega \approx 1$ for the total density parameter of the universe.

It should be noted that the discussion of this section does not encompass all of the alternatives to WIMPs. Although these other dark matter candidates offer intriguing explanations to the dark matter problem, the next chapter will focus on the experimental detection of WIMPs.

2 Searching for WIMPs

The search for WIMPs can be separated in three categories: indirect detection, direction detection, and WIMP creation [15]. Direct detection experiments search for the scattering of dark matter particles on atomic nuclei and will be the topic of this thesis from Chapter 3 onward. Indirect detection experiments search for remnants of WIMP annihilation such as gamma-rays, positrons, and neutrinos using both space based and ground based detectors. Similarly, high energy particle colliders such as the LHC are used to search for missing energy signals during WIMP that may be produced due to their collisions.

2.1 Indirect Detection Experiments

In section 1.2.3 we discussed the annihilation of CDM particles such as WIMPs during the early universe. The WIMP annihilation cross section must be close to $\sigma_\nu \sim 3 \times 10^{-26}$ cm^3/s to account for the observed abundance of dark matter, which provides a well defined target for indirect detection experiments. [32] WIMP annihilation may produce any standard model particle that is not kinematically forbidden. Numerous indirect detection experiments search for the gamma-ray, neutrino, and positron annihilation remnants in gravitational wells where the dark matter density is expected to be high, such a the center of the Sun, the center of the Milky Way, or the center of neighboring galaxies. In the following sections, we will discuss efforts to detect each of these annihilation products separately.

2.1.1 Gamma-Ray Experiments

If a WIMP (χ) annihilates directly into a photon (γ) and another particle (X), the photon is monoenergetic with an energy given by

$$E_\gamma = m_\chi \left(1 - \frac{m_X^2}{4m_\chi^2}\right) \tag{68}$$

where m_χ is the mass of the WIMP and m_X is the mass of the remnant particle. [?] At the GeV energy scale photons interact with matter via electron-positron pair production, leading to an interaction length much shorter than the thickness of Earth's atmosphere. As a result, any experiment seeking to directly detect gamma-ray radiation from WIMP annihilation must be based in space. Satellites such as the Fermi-LAT detect the electron-positron pairs produced by gamma-ray interaction in a detector made of a dense material (in the case of Fermi-LAT, tungsten is used). These space-based detectors are hindered by the numerous sources of background radiation present in astrophysical data, and are therefore unable to make significant claim of detection without observing a monoenergetic signal across multiple sources. Typically, gamma-ray detection experiments measure signals originating from dwarf galaxies, as they have relatively little backgrounds and are therefore ideal for searching for dark matter annihilation signals. As of 2012 the Fermi-LAT has observed no such line features or significant gamma-ray flux in its data [6].

When gamma-rays interact with the atmosphere they produce a cascade of secondary particles. These seconday particles produce Cerenkov radiation as they pass through the atmosphere, allowing ground-based telescopes to search for the gamma-ray product of WIMP annihilation indirectly. Cosmic ray radiation can also induce Cerenkov radiation in the atmosphere, making the it difficult to distinguish gamma-ray sources from the cosmic ray background. Ground based experiments employ numerical simulations of atmospheric showers and require an excess of directional gamma-rays above the isotropic background induced by cosmic rays to overcome this challenge [37]. As with space based experiments, ground based experiments have yet to observe a gamma-ray flux above background in their data [4].

2.1.2 Neutrino Experiments

Neutrinos from WIMP annihilation can interact with ordinary matter via a charge current interaction or a neutral current interaction. In a charged current interaction, a high energy neutrino transforms into its lepton partner via a process such as inverse beta decay

$$\bar{\nu_e} + p \rightarrow n + e^+. \tag{69}$$

These neutrino interactions are ideal to work with, since the leptons are easy to detect and allow the neutrino to be flavor-tagged. However, if a neutrino has less energy than the mass of its lepton partner it can not interact via a charge current interaction. In a neutral current interaction the neutrino remains as a neutrino but deposits energy and momentum onto a target particle. If the target is light, such as in the electron interaction

$$\bar{\nu_e} + e^- \rightarrow \bar{\nu_e} + e^-, \tag{70}$$

it can be accelerated above the speed of light in the medium and produce Cerenkov radiation.

Ground based detectors, such as ANTARES and IceCube, search for the neutrinos produced during dark matter annihilation in the Sun, where WIMPs would accumulate due to scattering on protons. The high energy neutrino signals would present as Cerenkov radiation produced by muon tracks in charged current interactions at the GeV-TeV energy scale, which would in turn be observed by large photo-multiplier arrays buried deep in a transparent medium, such as the antartic ice. Such a signal would be a strong indication of dark matter, since no other processes are expected to produce it.

Unlike direct detection experiments, where the spin-dependent scattering cross section is a function of the expectation values of the proton and neutron spin operators in the target nucleus, neutrino observation experiments can place strong limits on the spin dependent cross since they are directly measuring annihilation remnants. Such limits are strongly dependent on assumptions for the dark matter annihilation process, and are therefore more model-dependent than direct detection experiments. So far, neutrino observation experiments have not observed any dark matter annihilation signal from dark matter particles at the center of the Sun or in nearby galaxy clusters, but have set the world's best spin-dependent cross section limits for WIMPs in the process [2, 3].

2.1.3 Positron Experiments

Positrons can be produced with a varying spectrum via direct annihilation of dark matter to positron-electron pairs or by annihilations to ZZ or W^+W^- [19, 36]. These positrons do not travel in straight lines from their source due to galactic magnetic fields. Due to their low mass, electrons and positrons lose energy via inverse Compton scattering and synchrotron radiation as they travel from source to observer. The energy loss increases with the square of the electron energy, such that the power law energy spectrum is steepened at the location of the observer, resulting in an expectation of $\sim \mathrm{E}^{-3}$ [22].

The inelastic collision of cosmic-ray protons and α-particles produce charged pions, which in turn produce secondary positrons and electrons in roughly equal amounts via the $\pi - \mu - e$ decay chain [53]. For secondary electrons and positrons, the source spectrum would therefore follow the energy spectrum of ambient protons, which is approximately $\sim \mathrm{E}^{-3.7}$ after radiative loss during transit. If the only source of positrons was from secondary production, and astrophysical sources produced electrons, we would then expect the positron fraction $e^+/(e^+ + e^-))$ to decrease smoothly with energy [22]. Therefore, experiments which seek to measure a positron signal from dark matter annihilation observe the positron fraction as a function of energy from the entire galactic halo and compare their results to astrophysical models of positron production.

Experiments such as FERMI-LAT, PAMELA, and AMS-02 have confirmed a rise in the positron fraction at high energy [7, 24, 5]. However, a very high cross section and leptophilic models are required for these observations to be attributed to dark matter annihilation. Alternative explanations such as local pulsar sources and acceleration of secondary positrons have also been proposed [50].

2.2 WIMP creation in Colliders

Experiments such as ATLAS and CMS are using the Large Hadron Collider (LHC) beneath France and Switzerland to search for the production of WIMPs in high energy particle collisions. The LHC is a proton-proton collider which should have a large production cross section for colored super symmetric particles. The WIMP pair production interaction $pp(p\bar{p}) \to \chi\bar{\chi}$ is of no use in these experiments, since it leaves no observable signal in the detector. Instead, these experiments try to observe the higher order $pp \to \chi\bar{\chi} + jets$ interaction, with the jets serving as a trigger that an event took place. The dominant background when looking for such an event comes from the electroweak processes where the Z decays into a pair of neutrinos $pp(p\bar{p}) \to \nu\bar{\nu} + jets$ or the $W^{\pm}$ decays into a neutrino and a lepton $pp(p\bar{p}) \to l^{-}\bar{\nu} + jets$ or $pp(p\bar{p}) \to l^{+}\nu + jets$. In a WIMP + jets event the WIMP will exit the detector unseen, producing a signature with missing transverse momentum. The magnitude of this missing momentum is typically denoted as E_T^{miss}. A model-independent approach shows that E_T^{miss} should be detectable at the LHC under the assumption that all new particles mediating the interaction of WIMPs and standard model particles are too heavy to be produced directly [13]. However, no excess of events beyond the standard model processes has been observed at the LHC as of yet [1].

2.3 Direct Detection Experiments

If dark matter interacts through the weak force then it should be possible to observe WIMPs via nuclear recoils in direct detection experiments. During these events a WIMP will scatter off of a target nucleus in the detector, producing a nuclear recoil signal in the range of 1-100 keV [40]. Direct detection experiments typically observe ionization, scintillation, or low temperature phonons produced during the event (or a combination of the three), although some experiments have developed a method of detection based on producing bubbles in a superheated fluid at the site of a recoil. These signals are susceptible to both nuclear recoil and electron recoil backgrounds so detailed in situ calibrations are required to characterize the detector's response to each type of event. In this section, we will review the canonical galactic halo model and derive an expression for the WIMP recoil spectrum before discussing different types of direct detection experiments in detail. The following chapter we will be devoted to one particular direct detection experiment, the LUX detector.

2.3.1 The Canonical Halo Model

The canonical halo model treats dark matter as an isothermal spherical distribution that behaves as a non-interacting ideal gas. The spherical shape of the distribution implies no rotational movement in the bulk of the distribution, otherwise it would flatten into a disk. The velocity of a WIMP relative to the galactic center, v_0, can be approximated by the orbital velocity at a given radius from the galactic center. At the location of the sun, $r \approx 8.5$ kpc, and $v_0 \approx 220$ km/s [44].

The local number density of WIMPs is given by

$$n_\chi = \frac{\rho_\chi}{M_\chi} \tag{71}$$

where ρ_χ is the density of WIMPs in the local vicinity, and M_χ is the mass of a WIMP particle. The local density of the dark matter halo is estimated to be $0.3 < \rho_\chi < 0.7$ GeV/cm^3 [29]. Assuming the value of $\rho_\chi = 0.4$ GeV/cm^3 from reference [40] we see that $n_\chi = 0.004$ per cm^3 for a WIMP mass of 100 GeV. With an average WIMP velocity of $v_0 = 220$ km/s, this is equivalent to a flux of $\phi_\chi \approx 10^7 M_\chi$ s^{-1}cm^{-2}, or roughly half a billion WIMPs of $M_\chi = 100$ GeV passing through your hand every second.

2.3.2 The WIMP Recoil Spectrum

Lewin and Smith provide a standard derivation of the expected WIMP recoil spectrum in reference [40]. Their derivation begins with the differential particle density given by

$$dn = \frac{n_0}{k} f(\mathbf{v}, \mathbf{v_E}) d^3\mathbf{v} \tag{72}$$

where n_0 is the mean dark matter particle density, $\mathbf{v}$ is the velocity of the WIMP relative to the target, $\mathbf{v_E}$ is the velocity of the earth relative to the WIMP, $f(\mathbf{v}, \mathbf{v_E})$ is the WIMP velocity distribution function. The normalization constant k is given by

$$k = \int_0^{2\pi} \int_{-1}^{1} \int_0^{v_{esc}} f(\mathbf{v}, \mathbf{v_E}) v^2 d(cos\theta) dv \tag{73}$$

where v_{esc} is the local escape velocity, so that

$$\int_0^{v_e sc} dn \equiv n_0. \tag{74}$$

Note that an annual modulation is induced in the velocity of the earth relative to the dark matter particles, and subsequently induced in the event rate of WIMPs in terrestrial detectors as well, due to the velocity of earth around the sun. This modulation is given by

$$v_E = v_0 + 15 \cos\left(2\pi \frac{T - 152.5}{365.25}\right) \tag{75}$$

where T is measured in days from June 2nd, and $v_0 \approx 220$ km/s is the velocity of the sun around the galactic center. The DAMA/Libra collaboration has claimed a detection a dark matter signal with annual modulation with 8.2 σ significance. However, many dark matter experiments have since ruled this result out, so it is likely due some other unidentified modulating phenomenon in the data.

We treat the dark matter as a non-interacting ideal gas so that we can assume a Maxwellian dark matter velocity distribution given by

$$f(\mathbf{v}, \mathbf{v_E}) = e^{(-v+v_E)^2/v_0^2}. \tag{76}$$

Then for $v_{esc} = \infty$ we define

$$k_0 \equiv (\pi v_0^2)^{3/2}, \tag{77}$$

and for finite escape velocity $v_{esc} = |\mathbf{v} + \mathbf{v_E}|$,

$$k = k_0 \left[\mathrm{erf}(\frac{v_{esc}}{v_0}) - \frac{2}{\sqrt{\pi}} \frac{v_{esc}}{v_0} e^{-v_{esc}^2/v_0^2} \right]. \tag{78}$$

The event rate per unit mass on a target of atomic mass A (AMU), with cross-section per nucleus σ is given by

$$dR = \frac{N_0}{A} \sigma v dn \tag{79}$$

where N_0 is Avogadro's number (6.02×10^{23} mol^{-1}). For constant cross section $\sigma = \sigma_0$, the event rate per unit mass is then

$$R = \frac{N_0}{A} \sigma_0 \int v dn \equiv \frac{N_0}{A} \sigma_0 n_0 \langle v \rangle . \tag{80}$$

Substituting $n_0 = \rho_\chi / M_\chi$ (where ρ_χ and M_χ are the WIMP density and mass, respectively) we define the event rate per unit mass for $v_E = 0$ and $v_{esc} = \infty$ as

$$R_0 = \frac{2N_0\rho_\chi}{\sqrt{\pi}AM_\chi}\sigma_0 v_0 = \frac{2\rho_\chi}{\sqrt{\pi}M_\chi M_T}\sigma_0 v_0 \tag{81}$$

where M_χ is the mass of the WIMP and M_T is the mass of the target, such that

$$R = R_0 \frac{\sqrt{\pi}\,\langle v\rangle}{2v_0} = R_0 \frac{k_0}{2\pi v_0^4 k}\int v f(\mathbf{v}, \mathbf{v_E}) d^3v. \tag{82}$$

In differential form equation 82 becomes

$$dR = R_0 \frac{k_0}{2\pi v_0^4 k} v f(\mathbf{v}, \mathbf{v_E}) d^3v. \tag{83}$$

The recoil energy (as measured in the lab frame) of a nucleus struck by a WIMP of kinetic energy $E = \frac{1}{2}M_\chi v^2$ and scattered at an angle θ in a center-of-mass frame is given by

$$E_R = \frac{1}{2}M_\chi v^2 \frac{2M_\chi M_T}{(M_\chi + M_T)^2}(1 - \cos\theta). \tag{84}$$

For isotropic scattering recoils are uniformly distributed over a range of $0 \leq E_R \leq \frac{1}{2}M_\chi v^2 \frac{4M_\chi M_T}{(M_\chi+M_T)^2}$ so

$$\frac{dR}{dE_R} = \int_{E_{min}}^{E_{max}} \frac{(M_\chi + M_T)^2}{4M_\chi M_T E} dR(E) \tag{85}$$

where $E_{max} = \frac{1}{2}M_\chi v^2 \frac{4M_\chi M_T}{(M_\chi+M_T)^2}$ and E_{min} is the smallest WIMP energy which can produce a recoil of energy E_R. Since $E = \frac{1}{2}M_\chi v^2$ and $E_0 = \frac{1}{2}M_\chi v_0^2$, $E = E_0\frac{v^2}{v_0^2}$ and equation 85 becomes

$$\frac{dR}{dE_R} = \frac{(M_\chi + M_T)^2}{4M_\chi M_T E_0}\int_{v_{min}}^{v_{max}} \frac{v_0^2}{v^2} dR(v) \tag{86}$$

where v_{min} and v_{max} is the WIMP velocities corresponding to E_{min} and E_{max}. Therefore, using equations 77, 81, and 83 the expected energy recoil spectrum of WIMPs scattering off of a target nucleus is given by

$$\begin{aligned} \frac{dR}{dE_R} =& \frac{(M_\chi + M_T)^2}{4M_\chi M_T} \frac{k_0 R_0}{2\pi E_0 k v_0^2} \int_{v_{min}}^{v_{max}} \frac{f(\mathbf{v}, \mathbf{v_E})}{v} d^3v \\ =& \frac{(M_\chi + M_T)^2}{2M_\chi^2 M_T^2} \frac{\rho_\chi}{M_\chi} \frac{\sigma_0}{k} \int_{v_{min}}^{v_{max}} \frac{f(\mathbf{v}, \mathbf{v_E})}{v} d^3v \end{aligned} \tag{87}$$

It is conventional to express σ_0 as the product of σ_0 at the coherent scattering limit in which the WIMP interacts with the entire nucleus (with momentum tranfer $q = 0$) and a nuclear form factor F which accounts for the loss of coherence with higher momentum transfer. Therefore, using the WIMP-nucleus reduced mass given by $\mu \equiv \frac{M_\chi M_T}{M_\chi + M_T}$ equation 87 becomes

$$\frac{dR}{dE_R} = \frac{\sigma_0 \rho_\chi}{2\mu^2 M_\chi k} F^2(q) \int_{v_{min}}^{v_{max}} \frac{f(\mathbf{v}, \mathbf{v_E})}{v} d^3v, \tag{88}$$

where, as a reminder, ρ_χ is the local WIMP density, $f(\mathbf{v}, \mathbf{v_E})$ is the velocity distribution of WIMPs in the halo, v_{min} is the minimum WIMP velocity able to generate a recoil of energy E_R, v_{esc} is the escape velocity for WIMPs in the halo, σ_0 is the WIMP-nucleus interaction cross sections, and $F(q)$ is the nuclear form factor describing the scattering amplitude for momentum transfer q.

The WIMP-nucleus cross section can have both spin-independent (SI) and spin-dependent (SD) components [51]. The SI interaction cross section is given by

$$\sigma_0^{SI} = \frac{4}{\pi} \mu^2 \left[Z f_p + (A - Z) f_n \right]^2,$$

where Z is the atomic number of the target nucleus (the number of protons), A is the atomic mass number of the target nucleus ($A - Z$ is therefore the number of neutrons in the nucleus), and f_p and f_n are the effective scalar couplings of WIMPs to protons and neutrons, respectively. In this process we must sum over the interactions in each nucleon prior to squaring, since the DeBroglie wavelength associated with the momentum transfer is comparable to, or larger than, the size of the target nuclei, giving rise to a coherence effect across the nucleons. If the scalar couplings of WIMPs with neutrons and protons are approximately equal (which is the case with the LSP of SUSY), then the SI cross section can be simplified to

$$\sigma_0^{SI} \simeq \frac{4}{\pi}\mu^2 A^2 |f_p|^2.$$

The cross section for SD interactions is given by

$$\sigma_0^{SD} = \frac{32}{\pi} G_F^2 \mu^2 \frac{J+1}{J} \left[\langle S_p \rangle a_p + \langle S_n \rangle a_n\right]^2,$$

where G_F is the Fermi constant, J is the total spin of the target nucleus, $\langle S_{(p,n)} \rangle$ are the expectation values of the proton and neutron group spins, and $a_{(p,n)}$ are the effective SD WIMP couplings on protons and neutrons. In SD WIMP-nucleus interactions it is assumed that only unpaired nucleons contribute significantly to the total cross section, since the spins of the nucleons in a nucleus are anti-aligned. In most cases, the spin independent, coherent term dominates the total WIMP-nucleus cross section due to its A^2 dependence on the atomic mass number of the target nucleus.

A calculation of both the differential and integrated WIMP event rates in single isotope targets of ^{131}Xe, ^{73}Ge, and ^{40}Ar using a WIMP mass of 100 GeV is included in Figure 4.

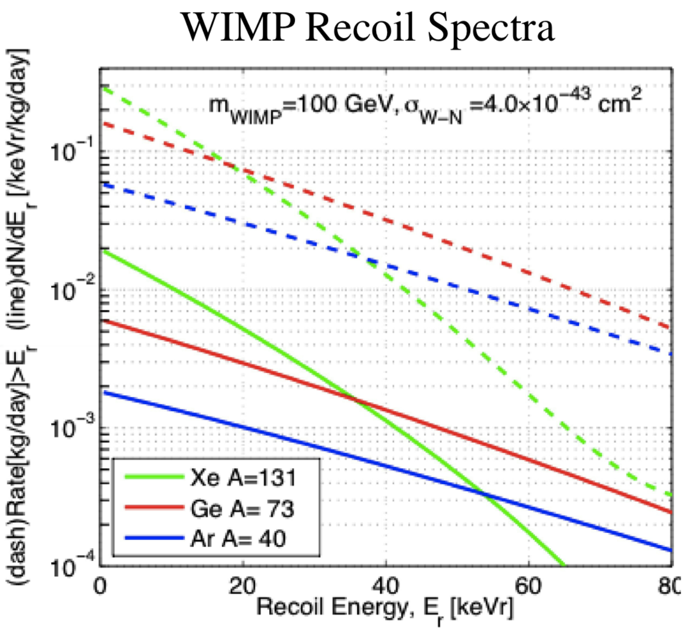

Figure 10: Calculated differential spectrum in evts/keV/kg/d (solid lines) and the integrated event rate in evts/kg/d (dashed lines) for ^{131}Xe, ^{73}Ge, and ^{40}Ar assuming a 100 GeV WIMP with spin-indepdent cross section for a WIMP-nucleon of $\sigma = 5 \times 10^{-43}$ cm^2.

Lighter target nuclei will produce lower event rates in a WIMP detector due to their lower cross sections (resulting from lower A^2 contribution in the coherent SI term) and less effective transfer of energy during nuclear recoil events from heavy WIMPs. While heavier target nuclei produce stronger interaction cross sections, they also result in reduced event rates at high energies due to a loss of coherence from form factor suppression. This loss of coherence is not enough to make light target nuclei more ideal than heavy target nuclei at high energies, but the event rate is not enhanced by as much as a naive A^2 scaling would suggest. To maximize efficiency a xenon detector with a low analysis threshold is ideal.

2.3.3 Backgrounds in Direct Detection Experiments

Direct detection experiments search for an extremely rare nuclear recoil signal between 1-100 keV. These detectors have a number of internal and external backgrounds which could obscure with the WIMP signal. Therefore, limiting sources of background is critical to maintaining a high discovery potential.

Internal backgrounds can be introduced by radioactive materials present in individual detector components. Naturally occurring radioisotopes such as ^{232}Th, ^{238}U, and ^{40}K can produce high energy gamma rays which penetrate deep into a detector. In the case of ^{232}Th, the decay chain produces high energy gamma rays from radioactive daughters such as ^{228}Ac, ^{212}Pb, ^{212}Bi, and ^{208}Tl before reaching stable ^{208}Pb. Likewise, the ^{238}U decay chain produce high energy gamma rays from ^{234}Th, ^{234}Pa, ^{214}Pb, ^{214}Bi before reaching stable ^{206}Pb. In the case of ^{40}K, a 1460.85 keV gamma ray is produced via electron capture decay to ^{40}Ar.

In addition to the naturally occurring radioisotopes, cosmogenically activated radioisotopes can also be present inside detector components. Neutron activation of copper can produce ^{60}Co, which produces 1.173 MeV and 1.33 MeV gamma rays when it beta decays into ^{60}Ni with a half life of 5.2714 years. Neutron activation of titanium produces ^{46}Sc, which emits 889 keV and 1.12 MeV gamma rays when it beta decays into ^{46}Ti via electron emission with a half life of 84 days.

Radon in the detector introduces the ^{222}Rn and ^{220}Rn decay chains as additional backgrounds. While most of the daughters in the radon decay chains produce easily vetoed alpha particles, the ^{222}Rn decay chain includes beta and gamma emitters such as ^{214}Pb and ^{214}Bi. ^{214}Pb decays into ^{214}Bi with a half life of 26.8 minutes via beta emission at 1024 keV, and the subsequent ^{214}Bi decays in ^{214}Po with a half life of 19.9 minutes via beta emission at 3272 keV. The ^{220}Rn decay chain includes ^{212}Pb, which decays into ^{212}Bi with a half life of 10.64 hours via beta emission at 573.8 keV. The ^{212}Bi then decays via alpha decay into ^{208}Tl, which can subsequently decay via beta emission. These beta decays either produce no gamma ray particles (referred to as "naked" beta decays) or high energy gamma rays that can leave the detector without scattering (refereed to as "semi-naked" beta decays), resulting in a background which can not be reduced via detection of a high energy gamma-ray component. Internal backgrounds from detector components are mitigated with careful screening of the materials which go into a detector; with simulations being used to predict background events arising from materials which make it through the screening process [18].

Long-lived intrinsic radioisotopes can be present in the detection medium as well. Cosmogenically activated ^{127}Xe beta decays via electron capture to ^{127}I with a half life of 36.358 days. The captured electron has an 85% chance of coming from the K shell with an x-ray of 33 keV, a 12% chance of coming from the L shell with an x-ray of 5.2 keV, and a 3% chance of coming from higher shells with x-rays of $<$1.2 keV. The subsequent ^{127}I daughter can decay to ground state via high energy gamma emission, with the gamma frequently leaving the detector without scattering. The ^{127}Xe activity decays away quickly, so this background can be mitigated by moving the detector underground prior to data collection. ^{39}Ar is generated by cosmic ray interactions with ^{40}Ar in a (n,2n) process in the atmosphere and can find its way into a detector's medium. The 565 keV electron emission decay has a half life of 269 years, placing strong constraints on the amount of ^{39}Ar that can be present in a detector's medium when data is collected. ^{85}Kr is produced by man-made processes, such as nuclear fuel re-processing. As with

^{39}Ar, the ^{85}Kr can make its way into a detector's medium where it will beta decay to ^{85}Rb with a half life of 10.756 years at 687 keV. These long lived radioisotopes which originate from the atmosphere must be purified from the detector medium prior to data collection to reduce background levels in the detector [18].

Neutrons are particularly dangerous source of background which can mimic the single scatter nuclear recoil present in a WIMP signal. While neutrons can be stopped by a few tens of meter water equivalent shielding, cosmic ray muons can penetrate many kilometers of shielding. Muon interactions in the laboratory can produce "cosmogenic" neutrons at the GeV scale with mean free path much longer than most detectors. These neutrons can be attenuated by rock or shielding and produce keV scale recoils in WIMP detectors. Such events are mitigated by tagging the initial muon with a muon veto system, placing external shielding around the detector, and by placing the detector deep underground to limit the muon flux. Neutrons can also be generated internally via (α,n) interactions in construction materials, such as the (α + ^{19}F $\rightarrow$ ^{22}Na + n) reaction in fluorine present in PTFE, and from spontaneous fission of ^{238}U and ^{232}Th.

The background mitigation techniques discussed in this section can not completely remove backgrounds from a detector. To separate any remaining backgrounds from a WIMP signal, detectors use a technique called nuclear recoil discrimination. Nuclear recoil discrimination does not reduce the total number of background events, but instead seeks to distinguish electron recoil interactions from nuclear recoil interactions and reject the former population. In the next section we discuss a variety of WIMP detection methods, with each of these methods having its own form of nuclear recoil discrimination.

2.3.4 Direct Detection Methods

Ionizing radiation deposits energy in a detector in the form of scintillation light, ionization, and heat. A variety of WIMP detectors have been constructed that each detect one or two of these channels. Scintillation detectors use scintillating crystals or liquid scintillators as a target medium. For instance, the DAMA/LIBRA experiment at the Gran Sasso Laboratory in Italy uses room temperature, thallium doped sodium iodide (NaI(Tl)) scintillating crystals as a target medium. Each crystal is paired with two photomultiplier tubes (PMT) which collect scintillation light from within each crystal. Annual modulation of the WIMP signal due to the motion of the earth around the sun is used to discriminated background events from WIMP events. The XMASS detector uses liquid xenon as a target medium. The scintillation produced in the xenon by recoil events is collected by PMT arrays. Background events from gamma ray sources are attenuated by the liquid xenon's large atomic number (Z=54) and high density, leading to a low background fiducial volume. This discrimination technique is referred to as "self shielding."

Single phase liquid argon experiments, such as DEAP and CLEAN, can not take advantage of self shield techniques due to the intrinsic background from ^{39}Ar. Instead, these experiments use a technique called pulse shape discrimination to differentiate signal events from background. Scintillation in liquid noble gases is produced by the decay of singlet or triplet excimers. The triplet state emits light over a longer period of time, and the light can be suppressed by destructive interactions such as Penning ionization and electron-triplet spin exchange. Nuclear recoils produce higher excitation densities, and therefore more destructive interactions with the triplet excimers, leading to a difference in the pulse shape of nuclear recoil and electron recoil events.

Single phase ionization detectors have also been used in the search for dark matter. The CoGeNT detector in the Soudan Underground Laboratory in Minnesota uses a low input capacitance p-type point contact (PPC) germanium crystal to detect ionization from WIMP interactions. The detector has energy thresholds as low as 500 eV, allowing the collaboration to search for low mass ($\sim$5 GeV/c^2) WIMP particles. Electron recoil background events scatter at multiple events sites in the germanium crystal, while WIMPs scatter at most once. This leads to a longer rise time in pulses from background events which can be used as another form of pulse shape discrimination.

Phonon detectors are the final type of single signal detectors. These type of detectors, such as the Cryogenic Underground Observatory for Rare Events (CUORE) in the Gran Sasso National Laboratory, use low heat capacity crystals as a target medium. In the case of CUORE, tellurium dioxide crystals (TeO_2) are held at 10 mK to reduce thermal noise. The low heat capacity of the crystals allows particle interactions to raise the temperature of the crystals, which in turn changes the resistance of neutron transmutation doped germanium thermistors which are glued to the top of each crystal. A constant current is applied to the thermistors, and the voltage across each thermistor is used as a detection method. These types of detectors do not have any means of event discrimination, so they rely heavily on the use of radiopure construction materials and background modeling.

In addition to the single signal detectors, many detectors collect data from two of the three energy deposition channels. The Cryogenic Dark Matter Search (CDMS) in the Soudan mine records signals from both phonons and ionization. The detector uses Ge and Si detectors cooled to $\sim$40 mK as a target medium. The low temperature is required to reduce thermal noise in the detector and to reduce the heat capacity of the target so that the temperature signal is large. Ionized electrons are drifted to the top of the crystals by an electric field where they are read out using field effect transistors, and the corresponding phonon signal is collected by superconducting transition edge sensors coupled with SQUIDs on the opposite face of each crystal. The ionization yield of a nuclear recoil is lower than an electron recoil, so the ratio of the two signals is used for nuclear recoil discrimination.

The Cryogenic Rare Event Search with Superconducting Thermometers (CRESST) is a phonon and scintillation detector in the Gran Sasso National Laboratory. CRESST uses calcium tungstate ($CaWO_4$) crystals, which are cooled to 10 mK to lower thermal noise, as a target medium. As with CDMS, transition edge sensors are used to detect phonons originating from particle interactions in the crystals. Scintillation light in the crystals absorbed by a silicon light absorber that converts the scintillation photons to heat, which are then detected by secondary thermometers. A nuclear recoil produces 10-40 times less scintillation light in the $CaWO_4$ crystals than an electron recoil does, so the ratio of the phonon and scintillation signal can be used for nuclear recoil discrimination.

The final class of detectors records the scintillation and ionization signals from particle interactions. These detectors, which are known as dual phase time projection chambers, use liquid noble scintillators (typically xenon or argon) as a target medium. Primary scintillation light is collected by PMT arrays at the top and bottom of the detector. An electric field is used to drift charge from ionized particles to the top of the detector, where the charge produces a secondary source of scintillation light as it accelerates through the gaseous xenon above the liquid.

The ratio of the primary and secondary scintillation light can be used for nuclear recoil discrimination. Currently, the most sensitive dark matter detector in the world is a dual phase TPC placed in the Sanford Underground Reasearch Facility in South Dakota. This detector, known as the Large Underground Xenon detector (LUX), will be discussed in depth in Chapter 3.

3 The LUX Detector

The Large Underground Xenon detector (LUX) is a dual phase time projection chamber location in the Sanford Underground Research facility in South Dakota. The detector is a dodecagonal structure that uses 300 kg of liquid xenon as a target medium. The commercially bought xenon was distilled to ~1 ppm (g/g) of air by the manufacturer before undergoing a krypton removal campaign to lower residual krypton levels to less than 5 parts per trillion (g/g). Particle interactions in the liquid xenon produce ionized and excited state xenon atoms. Some of the electrons released in the ionization process recombine with the xenon ions, forming additional xenon excitons, while the rest are drifted to the liquid surface by an electric field. The xenon excitons return to the ground state with a characteristic time constant of 2.2 ns for the singlet state and 27 ns for the triplet state, producing scintillation light at ~175 nm in the processes. This scintillation light is referred to as the S1 signal. Electrons which make it to the liquid surface are accelerated through the gas above the liquid xenon by a stronger electric field, producing electroluminescent light which is referred to as the S2 signal. This process will be discussed in depth in section **??** .

Two arrays of 61 PMTs each are used to measure both the S1 and S2 light in the detector. The light response of each PMT in the top array is used to reconstruct the XY position of recoil events based on the intensity of the S2 signal, and the time difference between the S1 and S2 signal is used to reconstruct the depth of the recoil events. In this way, the LUX detector has three dimensional position reconstruction which can be used to construct a low background fiducial volume in the3 center of the detector.

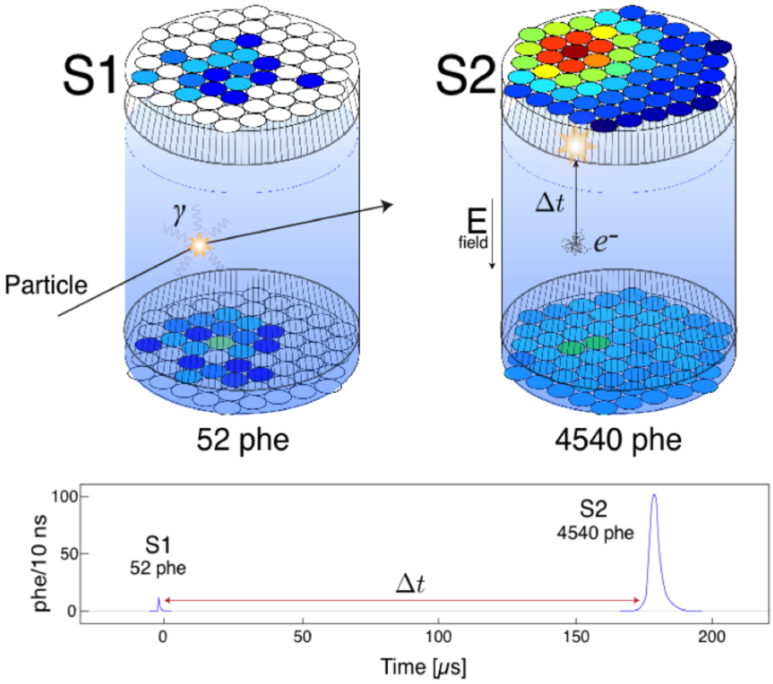

Figure 11: A depiction of a recoil event in LUX. The response of the top PMT array to the S2 light is used for xy position reconstruction, while the timing between the S1 and S2 signals is used for the depth measurement.

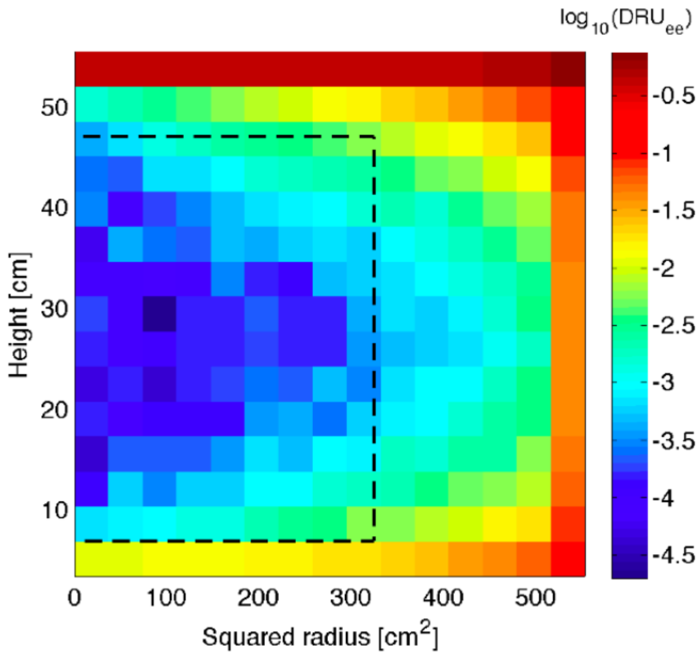

Figure 12: Simulated gamma ray backgrounds in the LUX detector after removing multiscatter events. The black dashed lines indicate the fiducial volume used in the first LUX WIMP search results.

The LUX detector is an extremely low background environment due to the strong self shielding properties of liquid xenon and the lack of naturally occurring xenon radioisotopes. Low energy external backgrounds (<50 keV) can only travel a few millimeters into the liquid xenon volume, while higher energy gamma rays (~MeV range) will produce easily identifiable multiscatter events due to their mean free path of a few centimeters. Any background events which do appear in the fiducial volume are reduced by over 99% by using the ratio of the S1 and S2 signal as a form of nuclear recoil discrimination. Discrimination techniques in the LUX detector will be discussed more in section **??**. In this section, we will discuss the detector internals, external support system, and the DAQ electronics used to read out the PMT signal.

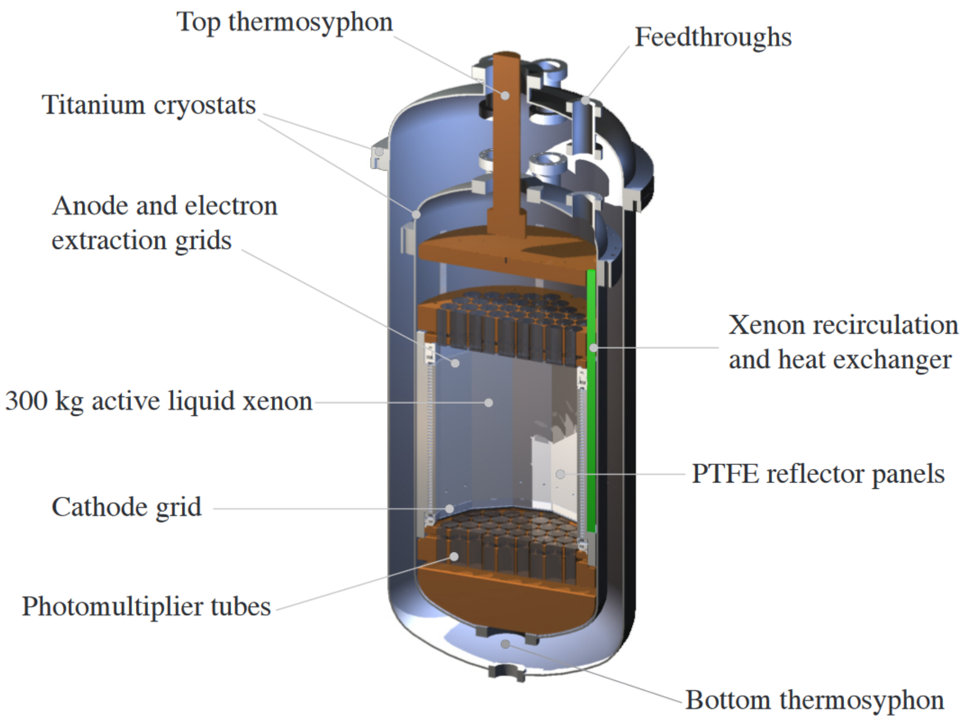

Figure 13: Cross section of the LUX cryostats and internal detector components [9].

3.1 Detector Internals

3.1.1 Cryostats

A cross section of the LUX cryostats and detector internals is shown in figure 13. An outer titanium cryostat is used to maintain a thermally insulating vacuum around the detector. An inner cryostat which houses the liquid xenon and detector internals is attached to the roof of the outer cryostat via three plastic hangers. Instrumentation cables and gas circulation plumbing are fed through flexible conduits at the top of the detector. Flexibility of the feedthroughs is required to deal with thermal contraction of the plastic hangers.

3.1.2 PMT Arrays, PTFE Structure, and Electric Field Cage

Inside the inner cryostat, a 5 cm thick copper block with a diameter of 55 cm is mounted directly on to the flange. This copper serves as a radiation shield and a temperature controller during detector operations. A similar copper structure is attached to the bottom of the inner cryostat and is used to displace xenon from the inactive volume in addition to the functions of the top radiation shield.

Two PMT arrays are used to collect light from the S1 and S2 signals in the detector. Each array contains 61 Hamamatsu R8778 PMTs which observe the active volume. These PMTs were specifically designed for operation in liquid xenon, with a typical quantum efficiency of 33% at the 175 nm wavelength of liquid xenon scintillation. The top PMT array is housed in a copper structure which is hung 15 cm below the upper radiation shield by six titanium straps. Reflective polytetrafluoroethylene (PTFE) trifoils cover the inner face of the copper housing to increase light collection efficiency in the detector. A similar structure is placed at the bottom of the detector to house the bottom PMT array.

Twelve PTFE panels hang from the top PMT support and are attached to the bottom PMT support. These panels are used to increase light collection efficiency in the detector, and serve as the support structure for the electric field cage in the detector. The field cage is made of five wire grids. Each grid is made of thing stainless streel wires and are 88-99% transparent at a normal angle of incidence. Stainless steel is known to be 57% reflective at xenon scintillation wavelength, further minimizing the optical footprint of the wire grids. The top grid is located 2 cm below the top PMT array. A stainless steel ring is used to string 50 micron diameter stainless steel wires spaced with a pitch of 1 cm. The voltage on the top grid is used to zero the electric field at the photocathodes of the top PMTs. The anode is placed 4 cm below the top grid. It is similar in design to the top grid, but uses 30 micro wires with 0.5 mm spacing. The gate grid, which uses 50 micron stainless steel wires with a pitch of 5 mm, is placed 1 cm below the anode grid. The position of the gate grid places it about 5 mm below the liquid xenon surface. These two grids work in tandem to produce a strong extraction field (5-6 kV/cm) that pulls charge out of the liquid xenon and into the gas, producing the S2 signal. The cathode grid is placed about 49.5 cm below the liquid surface. This grid uses 260 micron diameter stainless steel wires with a pitch of 5 mm, and works in tandem with the anode grid to produce a $\sim$180 V/cm electric field which drifts charge from a particle interaction to the liquid surface. The bottom grid is the last of the five wire grids. It is located 4 cm below the cathode grid and 2 cm above the bottom PMT support, and uses 206 micron diameter stainless steel wires with a pitch of 1 cm. The bottom grid serves the similar purpose as the top grid – it is used to zero the field at the photocathodes of the bottom PMT arrays.

Fourty-eight copper field rings are spaced 1 cm apart inside of the PTFE panels to shape the drift field. These rings have thickness of 3.2 mm and a width of 12.7 mm. The spacing and thickness of the rings were chosen to shield the active region from the electric field produced by the cathode high voltage cable. The voltage of the field rings is set by a resistor chain that runs between the gate and the cathode grids. A pair of 0.875 GΩ resistors connect the top field ring to the gate grid, while a pair of 1.25 GΩ resistors connect the bottom field ring to the cathode grid. A pair of 1 GΩ resistors is used to connect each adjacent field ring.

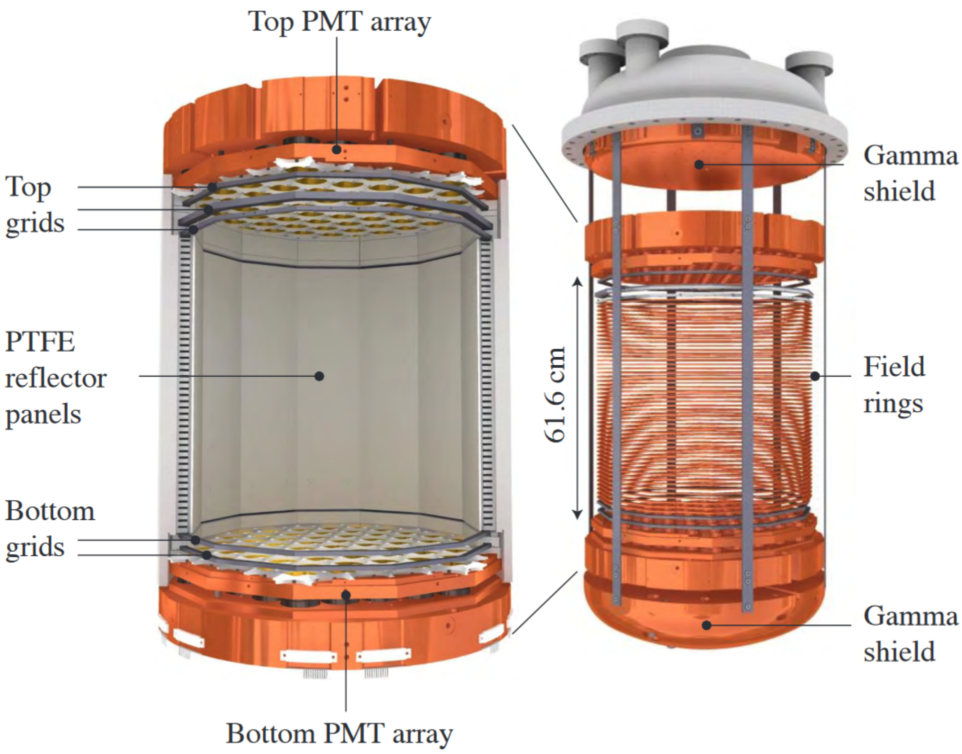

Figure 14: Depiction of the LUX PMT supports, PTFE panels, and field cage [9].

3.1.3 Cryogenics

A thermosyphon system is used to cool the detector internals to liquid xenon temperatures (∼175K) during operation. A thermosyphon is a sealed tube filled with a variable amount of gaseous nitrogen (N_2). A condenser which is immersed in a bath of liquid nitrogen is placed at the top of the thermosyphon. As the nitrogen in the thermosyphon tube condenses, gravity causes it to trickle down stainless steel plumbing to copper heat exchangers that are attached to various points in the inner cryostat. The condensed nitrogen evaporates when it hits the copper heat exchanger, removing heat from the detector. The evaporated nitrogen rises back up the stainless steel plumbing where it is once again condensed by the liquid nitrogen bath. In this way, the thermosyphons act in a continuous loop, transferring heat from the detector to the liquid nitrogen bath which the condenser is immersed in.

Two thermosyphons are attached to the copper radiation shields at the top and bottom of the inner cryostat and are used as the driving force to cool the detector from room temperature to 175K. Two more thermosyphons are attached to copper shielding around the inner inner cryostat and are used to prevent any thermal gradients from building in the detector. Each copper evaporator is fitted with a 50 W heater and a thermometer for fine temperature control. Larger 750 W heaters are attached to the two primary thermosyphons to aid in detector warm up during liquid xenon recovery.

3.1.4 Instrumentation

The LUX detectors is fitted with numerous instruments that help monitor and stabilize the conditions within the cryostat. Fourty 100 Ω thin film platinum resistance temperature detectors (RTDs) are used to monitor the temperature inside the inner cryostat. These instruments are help prevent the formation of thermal gradients which could warp the detector internals. An additional 23 RTDs are used to monitor the temperature inside the outer vacuum space, providing a means to detect leaks from the inner cryostat or outer atmosphere to the insulating vacuum space. Calibration of the RTD readouts was performed prior to installation, as well as in situ at room temperature, with an accuracy of 170 mK for each RTD. Advantech Adam 6015 modules are used to feed the output voltage of the RTDs to a slow control database, where multiple users can monitor the read outs and set automated alarms to notify collaboration members of any temperature fluctuations in the detector.

A variety of pressure sensors are used throughout the detector. Sensor models include Ashcroft AST4900 sensors, InstruTech Hornet ion and convection gauge, Swagelok PGU-50-PC100-L4FSF manual pressure gauges, and a Setra model 759 capacitance manometer. These instruments are used to monitor the stability of the inner cryostat, the quality of the outer vacuum, and the pressure in various locations of the gas circulation system. As with the RTDs mentioned above, all of the digital pressure gauges are read out to the slow control database where alarms can be set to notify users of potential leaks in the circulation system or out of control warming and cooling effects in the detector.

Six parallel wire sensors are used to monitor the liquid level in the inner cryostat, the weir, dual-phase heat exchanger, and the liquid return line. The later detectors mentioned here will be discussed in section 3.2.1. The capacitance of each wire pair depends on the length of wire submerged in the liquid, allowing the overall height of the liquid to be determined. Additionally, three parallel plate sensors are placed 120 degrees apart between the gate and anode grids. These sensors ensure the liquid surface is uniform and without any tilt.

3.2 External Support Systems

3.2.1 Gas Circulation and Purification System

The xenon used in the LUX detector needs to be free of electronegative and molecular impurities that could attenuate charge and light from particle interactions. To achieve this goal LUX circulates the detector's xenon through a gas system which includes a heated zirconium getter made by SAES. The getter removes nearly all non-nobel gas impurities with an efficiency of 99.9%, but requires the xenon to be in gaseous form when operating.

The process of evaporating the liquid xenon, flowing the gaseous xenon to the SAES getter, and recondensing the xenon before to returning it to the inner cryostat is handled by the LUX gas system. Within the inner cryostat excess liquid spills over the lip of a weir into a reservoir, where it enters the evaporator side of a two phase heat exchanger. In this side of the heat exchanger, xenon is pumped on by the external circulation system until it evaporates. The cooling effect of the evaporation is used to recondense xenon which is returning to the detector on the other side of the heat exchanger, reducing the heat load of the process by 90% **??**.

The gaseous xenon leaving the evaporator side of the heat exchanger passes through a concentric-tube heat exchanger which warms it to room temperature before circulating to the SAES getter. After passing through the SAES gettter, the purified xenon continues on to a second concentric-tube heat exchanger where it is cooled before entering the condenser side of the two phase heat exchanger. After condensing in the two phase heat exchanger the, now liquid, xenon enters the inner cryostat through the bottom radiation shield to ensure its temperature is consistent with the detector internals.

A diaphragm pump which is capable of 50 SLPM (420 kg/day) is used to maintain a constant flow of xenon through the circulation system. In practice, the flow is limited to $\sim$27 SLPM (227 kg/day) by the output pressure of the circulation pumps.

3.2.2 Gas Sampling System

Five xenon sampling ports are including in the gas circulation system. These ports allow xenon from the two phase heat exchanger, getter input, getter output, conduit purge lines, or circulation pump inlet to be diverted to a xenon assay system. The assay system makes use of a cryogenic cold trap to separate impurities from the xenon. During use, a xenon sample flows through the cold trap, where it is frozen through contact with a liquid nitrogen bath. The frozen xenon sets the vapor pressure of the system at 1.8 mTorr. Most impurities have a vapor pressure higher than 1.8mTorr, allowing them to pass through the cold trap and separate from the bulk of the xenon. The remaining impurities flow at high leak rates to a commercial Residual Gas Analyzer (RGA) made by SRS, where the absolute level of impurities in the bulk xenon is deduced by comparing to a calibration data set. After sampling, xenon can be discarded with the use of vacuum pumps in the sampling system, or recovered to high pressure cryogenic storage and recovery vessel (SRV) for potential reuse later. While we are most concerned with the krypton concentration due to the background producing radioisotope ^{85}Kr, it is important to assay the other impurities as well. Argon can produce radioactive backgrounds in the detector, helium can diffuse through PMT faces and damage the vacuum behind them, and nitrogen and oxygen can serve as an indicator for air leaks. This assaying technique results in sensitivity to krypton below 1 ppt (1e-12) g/g, a factor of 10,000 better than measurements performed without a cold trap.

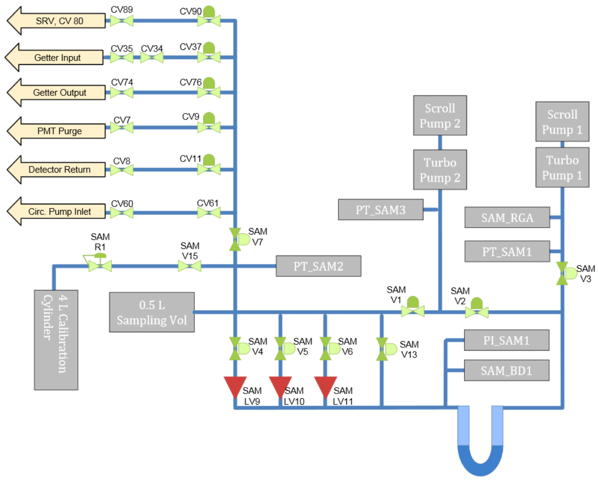

Figure 15: Depiction of the LUX sampling system. Xenon enters the sampling system through various sampling ports in the main circulation path. These sampling ports are shown in the top left of the diagram. The xenon then passes through one of three leak valves (indicated by red triangles) into a U-shaped cold trap, where it is analyzed by an RGA on the output of the cold trap. A secondary set of vacuum pumps is included so that the system can be evacuated independently of the RGA space.

3.2.3 Water Tank and Muon Veto System

The LUX cryostat is enclosed in a 7.6 meter diameter, 5.1 meter high water tank. The water tank holds 8 tons of water that is continuously circulated through an industrial purifying system to reduce detector backgrounds originating from the water tank itself. The concentration of uranium, thorium, and potassium are held more than six orders of magnitude lower than the rock surrounding the laboratory (2 ppt, 3ppt, and 4 ppb respectively). The water tank provides 2.75 m of shielding to the top of the detector, and 3.5 m of shielding to the sides, that reduces backgrounds originating in the laboratory environment. The tank is also outfitted with 20 Hammamatsu R7081 PMTs which can be used as an active veto for events which coincide with muons passing through the detector.

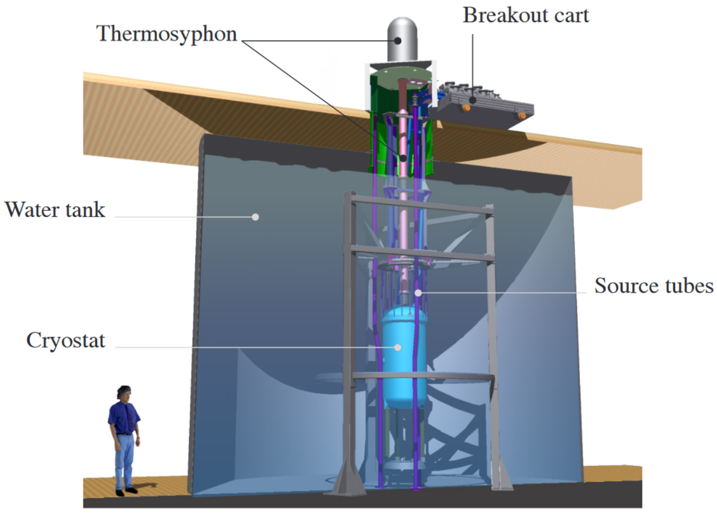

Figure 16: Cross section of the LUX water tank which surrounds the cryostat.

3.2.4 Calibration Systems

LUX utilizes multiple internal and external calibration sources to measure the detector's S1 and S2 response to recoil events. Six source tubes surround the cryostat in the water tank. A system of pulleys is used to temporarily deploy radioactive sources in each tube. A collimator is used for directional control of the particle interactions from the external sources. AmBe and ^{252}Cf are placed in the source tubes to calibrate the detectors nuclear recoil response. High energy ^{137}Cs gamma ray sources are placed in the tubes to calibrate the detector's electron recoil response, and to illuminate the detector walls for position reconstruction and background modeling studies. Other gamma ray sources, such as ^{22}Na and ^{208}Tl are available for electron recoil response calibration as well. High energy gamma rays from external sources only penetrate the outermost centimeters of the liquid xenon volume due the same self shielding properties that reduce unwanted external backgrounds, making it difficult to calibrate the entire fiducial volume with external sources.

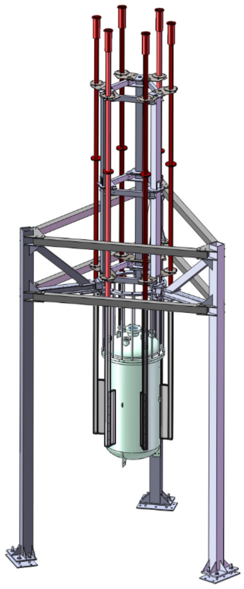

Figure 17: Rendering of the six external source tubes which surround the LUX cryostat.

In addition to the source tubes mentioned above, a 377 cm long horizontal air filled conduit can be lowered into the water tank by a pulley system. This conduit serves to displace water from the tank, opening a collimation path for an Adelphi Technologies,Inc. DD108 deuterium-deuterium neutron generator which is located outside of the water tank. The neutron generator is operated at a 5% duty cycle using 100 μs neutron pulses to produce mono-energetic 2.45 MeV neutrons at a rate of 500 Hz. The resulting neutrons scatter multiple times in the fiducial volume, and are used to calibrate the detector's nuclear recoil response from 0.7 to 24.2 keV$_{nr}$.

LUX also employs two internal calibrations sources which are injected directly into the gas circulation system. ^{83}Rb soaked charcoal is used to inject ^{83m}Kr directly into the circulation system on a weekly basis. ^{83}Rb decays into ^{83m}Kr with an 86.2 day half life. The resulting ^{83m}Kr daughter decays via internal conversion at 9.4 keV and 32.1 keV with a half life of 1.86 hours. Once injected into the gas system, the ^{83m}Kr quickly makes its way into the fiducial volume, where it uniformly disperses throughout the entire detector. The spatial uniformity and intrinsic nature of this source makes it extremely useful when measuring the spatial dependence of the detector's S1 and S2 signals, which we will be discuss in depth in Chapter **??**. After a calibration has finished, the ^{83m}Kr is removed from the detector in a short amount of time due to its 1.86 hour half life.

Tritiated methane (CH_3T) is the second internal calibration source used in LUX. CH_3T is a beta source with a peak at 2.5 keV and a mean energy of 5.6 keV. The wide, low energy spectrum of CH_3T is used to calibrate the detector's electron recoil response across the entire energy range of interest for WIMP events. CH_3T has a half life of 12.3 years, so unlike the ^{83m}Kr it must be actively removed from the detector by the SAES getter in the circulation system. The unprecedented CH_3T source was designed specifically for LUX, and is discussed in detail in Chapter **??**.

3.3 Detector Electronics

The photons collected by the two PMT arrays are amplified by the PMT dynode chains to mV scale voltage signals. The rise time for an S1 pulse is limited to $\sim$6 ns by the response of the PMTs, and the 29 ns effective time constant of the xenon excimer relaxation defines the S1 pulses' decay constant. The pulse width of and S2 event varies with depth due to diffusion of the electron cloud as it drifts through the detector.

The LUX data acquisition (DAQ) system is designed to distinguish >95% of single photoelectron pulses at 5 sigma above baseline noise fluctuations, and to prevent saturation of events with energies <100 keV$_{ee}$ at any stage in the electronics. To achieve this, the analog chain must put the peak of single photoelectron distribution at 30 ADC counts. In the analog chain, the mV scale signals from the PMTs are sent to a x5 amplitude preamplifier before passing to a post amplifier in the DAQ electronics rack. The multichannel post amplifier produces a gain of 1.5x that is sent to sixteen 8-channel ADC modules, and a gain of 2.8x to a DDC-8 trigger system.

The ADC modules digitize the signals at 100 MHz (10 ns/sample) with a resolution of 14 bits. Each ADC board is connected to a VME bus that is subsequently connected to the DAQ computer by fiber optic cables. Data is downloaded to the DAQ computer with speeds of up to 80 MB/s. Each ADC board is controlled by four field programmable gate arrays (FPGAs) that operate in a space saving "pulse only digitization" (POD) mode. In POD mode, PMT channels are paired and data is only saved to the DAQ computer if either member of the PMT pairing rises above threshold. A valid pulse trigger gate (VPTG) mechanism further reduces memory space demands. The VPTG is implemented using CAEN V814 discriminators which require two fold coincidence between PMT channels. Valid pulses are expected to occur in more than one channel, so the VPTG reduces unwanted triggers from various sources of noise.

The DAQ trigger system uses two 8 channel digital signal processors (DDC-8DSP). Top and bottom PMTs are summed into 16 groups (8 groups per array), and the analog sum of each group is produced with a Lecroy 628 Linear Fan-In/Fan-Out module. A trigger builder is connected to the DDC-8's and takes <1 μsecond to generate a final trigger signal to send to the DAQ. The trigger builder is capable of distinguishing S1 and S2 pulses, and can therefore operate in S1-only, S2-only, or S1 and S2 trigger mode. The DAQ can operate with a maximum trigger rate of 1.5 kHz before incurring deadtime.

3.4 Science Results

PUT RUN04 RESULT IF (OR RUN03 IF RUN04 ISNT AVAILABLE)

References

[1] Georges Aad, Tatevik Abajyan, Brad Abbott, Jalal Abdallah, S Abdel Khalek, AA Abdelalim, O Abdinov, R Aben, B Abi, M Abolins, et al. Search for dark matter candidates and large extra dimensions in events with a jet and missing transverse momentum with the atlas detector. *Journal of High Energy Physics*, 2013(4):1–51, 2013.

[2] Mark Gerald Aartsen, R Abbasi, Yasser Abdou, M Ackermann, J Adams, JA Aguilar, M Ahlers, D Altmann, J Auffenberg, X Bai, et al. Search for dark matter annihilations in the sun with the 79-string icecube detector. *Physical review letters*, 110(13):131302, 2013.

[3] MG Aartsen, R Abbasi, Yasser Abdou, M Ackermann, J Adams, JA Aguilar, M Ahlers, D Altmann, J Auffenberg, X Bai, et al. Icecube search for dark matter annihilation in nearby galaxies and galaxy clusters. *Physical Review D*, 88(12):122001, 2013.

[4] A Abramowski, F Acero, F Aharonian, AG Akhperjanian, G Anton, A Barnacka, U Barres De Almeida, AR Bazer-Bachi, Yvonne Becherini, J Becker, et al. Search for a dark matter annihilation signal from the galactic center halo with hess. *Physical Review Letters*, 106(16):161301, 2011.

[5] L Accardo, M Aguilar, D Aisa, B Alpat, A Alvino, G Ambrosi, K Andeen, L Arruda, N Attig, P Azzarello, et al. High statistics measurement of the positron fraction in primary cosmic rays of 0.5–500 gev with the alpha magnetic spectrometer on the international space station. *Physical review letters*, 113(12):121101, 2014.

[6] M Ackermann, Marco Ajello, A Albert, L Baldini, G Barbiellini, K Bechtol, R Bellazzini, B Berenji, RD Blandford, ED Bloom, et al. Fermi lat search for dark matter in gamma-ray lines and the inclusive photon spectrum. *Physical Review D*, 86(2):022002, 2012.

[7] M Ackermann, Marco Ajello, A Allafort, WB Atwood, L Baldini, G Barbiellini, D Bastieri, K Bechtol, R Bellazzini, B Berenji, et al. Measurement of separate cosmic-ray electron and positron spectra with the fermi large area telescope. *Physical Review Letters*, 108(1):011103, 2012.

[8] C Afonso, JN Albert, J Andersen, R Ansari, É Aubourg, P Bareyre, JP Beaulieu, G Blanc, X Charlot, F Couchot, et al. Limits on galactic dark matter with 5 years of eros smc data. *Astronomy & Astrophysics*, 400(3):951–956, 2003.

[9] DS Akerib, X Bai, S Bedikian, E Bernard, A Bernstein, A Bolozdynya, A Bradley, D Byram, SB Cahn, C Camp, et al. The large underground xenon (lux) experiment. *Nuclear Instruments and Methods in Physics Research Section A: Accelerators, Spectrometers, Detectors and Associated Equipment*, 704:111–126, 2013.

[10] Charles Alcock, RA Allsman, David R Alves, TS Axelrod, Andrew C Becker, DP Bennett, Kem H Cook, N Dalal, Andrew John Drake, KC Freeman, et al. The macho project: microlensing results from 5.7 years of large magellanic cloud observations. *The Astrophysical Journal*, 542(1):281, 2000.

[11] Varouzhan Baluni. Cp-nonconserving effects in quantum chromodynamics. *Physical Review D*, 19(7):2227, 1979.

[12] KG Begeman, AH Broeils, and RH Sanders. Extended rotation curves of spiral galaxies: Dark haloes and modified dynamics. *Monthly Notices of the Royal Astronomical Society*, 249(3):523–537, 1991.

[13] Maria Beltran, Dan Hooper, Edward W Kolb, Zosia AC Krusberg, and Tim MP Tait. Maverick dark matter at colliders. *Journal of High Energy Physics*, 2010(9):1–17, 2010.

[14] Alexey Belyanin. Physics of stellar interiors. `http://people.physics.tamu.edu/belyanin/astr314/lecture11.pdf`. Accessed: 2016-06-27.

[15] Gianfranco Bertone, Dan Hooper, and Joseph Silk. Particle dark matter: Evidence, candidates and constraints. *Physics Reports*, 405(5):279–390, 2005.

[16] Amitai Yisrael Bin-Nun. Gravitational lensing with a large deflection angle as a probe of general relativity and the galactic center. *Publicly accessible Penn Dissertations*, 2010.

[17] Tremaine Binney. *Galactic Dynamics*. Princeton University Press, 2 edition, 2008.

[18] P Brás. *Finding a needle in a haystack: Background studies and WIMP detection efficiency in LUX*. PhD thesis, Universidade De Coimbra, 2015.

[19] Hsin-Chia Cheng, Jonathan L Feng, and Konstantin T Matchev. Kaluza-klein dark matter. *Physical Review Letters*, 89(21):211301, 2002.

[20] Daniel JH Chung, Edward W Kolb, and Antonio Riotto. Superheavy dark matter. *Physical Review D*, 59(2):023501, 1998.

[21] Douglas Clowe, Maruša Bradač, Anthony H Gonzalez, Maxim Markevitch, Scott W Randall, Christine Jones, and Dennis Zaritsky. A direct empirical proof of the existence of dark matter. *The Astrophysical Journal Letters*, 648(2):L109, 2006.

[22] PEBS Collaboration. Positron fraction. `http://www1b.physik.rwth-aachen.de/~pebs/?PEBS_physics:Positron_fraction`, 2010. Accessed: 2016-06-14.

[23] Planck Collaboration et al. Planck 2015 results. xiii. cosmological parameters. arxiv preprint. *arXiv*, 1502, 2015.

[24] The PAMELA Collaboration. The cosmic-ray positron energy spectrum measured by pamela. *Physical Review Letters*, 111(1):081102, 2013.

[25] Darren J Croton. Damn you, little h!(or, real-world applications of the hubble constant using observed and simulated data). *Publications of the Astronomical Society of Australia*, 30:e052, 2013.

[26] Battaner E. and Florido E. The rotation curve of spiral galaxies and its cosmological implications. *Fund.Cosmic Phys.*, 21:1–154, 2000.

[27] John Ellis, John S Hagelin, Dimitri V Nanopoulos, K Olive, and Mark Srednicki. Supersymmetric relics from the big bang. *Nuclear Physics B*, 238(2):453–476, 1984.

[28] Chris Flynn, Andrew Gould, and John N Bahcall. Hubble deep field constraint on baryonic dark matter. *The Astrophysical Journal Letters*, 466(2):L55, 1996.

[29] Evalyn I Gates, Geza Gyuk, and Michael S Turner. The local halo density. *The Astrophysical Journal Letters*, 449(2):L123, 1995.

[30] H Goldberg. Constraint on the photino mass from cosmology. *Physical Review Letters*, 50(19):1419, 1983.

[31] S. Golwala. *Exclusion Limits on the WIMP-Nucleaon Elastic-Scattering Cross Section from the Cryogenic Dark Matter Search.* PhD thesis, University of Chicago, 2000.

[32] Dan Hooper and Lisa Goodenough. Dark matter annihilation in the galactic center. *Physics Letters B*, 697(5):412–428, 2011.

[33] Wayne Hu. Cmb introduction. `http://background.uchicago.edu/~whu/intermediate/map1.html`, 2001. Accessed: 2016-06-14.

[34] D. Javorsek, II, E. Fischbach, and V. Teplitz. New Experimental Bounds on the Contributions to the Cosmological Density Parameter Ω from Strongly Interacting Massive Particles. *The Astrophysical Journal*, 568:1–8, March 2002.

[35] Gerard Jungman, Marc Kamionkowski, and Kim Griest. Supersymmetric dark matter. *Physics Reports*, 267(5):195–373, 1996.

[36] Marc Kamionkowski and Michael S Turner. Distinctive positron feature from particle dark-matter annihilations in the galatic halo. *Physical Review D*, 43(6):1774, 1991.

[37] J Knapp, D Heck, SJ Sciutto, MT Dova, and M Risse. Extensive air shower simulations at the highest energies. *Astroparticle Physics*, 19(1):77–99, 2003.

[38] EW Kolb and MS Turner. The early universe, 1994.

[39] Hannu Kurki-Suonio. Lecture notes in cosmological perturbation theory. `http://theory.physics.helsinki.fi/~cpt/Cosmo12.pdf`, Fall 2015. Accessed: 2016-06-14.

[40] JD Lewin and PF Smith. Review of mathematics, numerical factors, and corrections for dark matter experiments based on elastic nuclear recoil. *Astroparticle Physics*, 6(1):87–112, 1996.

[41] Stephen J. Parke. Determining the neutrino mass hierarchy. In *Third NO-VE International Workshop on Neutrino Oscillations in Venice : Fifty years after the neutrino esperimental discovery : Venezia, February 7-10, 2006, Istituto Veneto di Scienze, Lettere ed Arti, Campo Santo Stefano*, pages 115–125, 2006.

[42] Sergio Pastor. Light neutrinos in cosmology. *Physics of Particles and Nuclei*, 42(4):628–640, 2011.

[43] M. Persic, P. Salucci, and F. Stel. The universal rotation curve of spiral galaxies - I. The dark matter connection. *Monthly Notices of the Royal Astronomical Society*, 281:27–47, July 1996.

[44] Til Piffl, C Scannapieco, J Binney, Matthias Steinmetz, R-D Scholz, MEK Williams, RS de Jong, G Kordopatis, G Matijevič, O Bienaymé, et al. The rave survey: the galactic escape speed and the mass of the milky way. *Astronomy & Astrophysics*, 562:A91, 2014.

[45] S Pires, J-L Starck, and A Refregier. Light on dark matter with weak gravitational lensing. *arXiv preprint arXiv:0908.4157*, 2009.

[46] Alexandre Refregier. Weak gravitational lensing by large-scale structure. *Ann.Rev.Astron.Astrophys*, 41:645–668, 2003.

[47] RG Hamish Robertson. Direct determination of neutrino mass. In *Journal of Physics: Conference Series*, volume 173, page 012016. IOP Publishing, 2009.

[48] Leslie J Rosenberg. Dark-matter qcd-axion searches. In *Journal of Physics: Conference Series*, volume 203, page 012008. IOP Publishing, 2010.

[49] Barbara Sue Ryden. *Introduction to cosmology*, volume 4. Addison-Wesley San Francisco USA, 2003.

[50] Pasquale D Serpico. Astrophysical models for the origin of the positron "excess". *Astroparticle Physics*, 39:2–11, 2012.

[51] Chung-Lin Shan. Determining ratios of wimp-nucleon cross sections from direct dark matter detection data. *Journal of Cosmology and Astroparticle Physics*, 2011(07):005, 2011.

[52] David N Spergel, Licia Verde, Hiranya V Peiris, E Komatsu, MR Nolta, CL Bennett, M Halpern, G Hinshaw, N Jarosik, A Kogut, et al. First year wilkinson microwave anisotropy probe (wmap) observations: determination of cosmological parameters. *The Astrophysical Journal Supplement Series*, 148(1):175, 2003.

[53] FW Stecker. The cosmic γ-ray spectrum from secondary particle production in cosmic-ray interactions. *Astrophysics and Space Science*, 6(3):377–389, 1970.

[54] David Tytler, David Kirkman, John M O'Meara, Nao Suzuki, Adam Orin, Dan Lubin, Pascal Paschos, Tridivesh Jena, Wen-Ching Lin, Michael L Norman, et al. Cosmological parameters sigma8, the baryon density, and the uv background intensity from a calibrated measurement of h i lyman-alpha absorption at z = 1.9. *The Astrophysical Journal*, 617(1):1, 2004.

[55] Jan van Paradijs and Johan AM Bleeker. X-ray spectroscopy in astrophysics. In *X-Ray Spectroscopy in Astrophysics*, volume 520, 1999.

[56] Alexey Vikhlinin, A Kravtsov, W Forman, C Jones, M Markevitch, SS Murray, and L Van Speybroeck. Chandra sample of nearby relaxed galaxy clusters: Mass, gas fraction, and mass-temperature relation. *The Astrophysical Journal*, 640(2):691–709, 2006.

[57] Xiang-Ping Wu, Tzihong Chiueh, Li-Zhi Fang, and Yan-Jie Xue. A comparison of different cluster mass estimates: consistency or discrepancy? *Monthly Notices of the Royal Astronomical Society*, 301(3):861–871, 1998.

[58] Anthony Zee. *Einstein gravity in a nutshell.* Princeton University Press, 2013.

[59] F. Zwicky. Republication of: The redshift of extragalactic nebulae. *General Relativity and Gravitation*, 41:207–224, January 2009.